SUPPLEMENTING LOCALIZATION ALGORITHMS FOR INDOOR FOOTSTEPS

AMERICO GIULIANO WOOLARD

Dissertation submitted to the faculty of the Virginia Polytechnic Institute and State University in partial fulfillment of the requirements for the degree of

DOCTOR OF PHILOSOPHY

IN

MECHANICAL ENGINEERING

PABLO A. TARAZAGA, CHAIR
R. MICHAEL BUEHRER, CO-CHAIR
ANDREW J. KURDILA
KEVIN B. KOCHERSBERGER
MARK S. CRAMER

July 7th, 2017
Blacksburg, Virginia

Keywords: localization, footsteps, structural health monitoring, dispersion, indoor wave propagation

SUPPLEMENTING LOCALIZATION ALGORITHMS FOR INDOOR FOOTSTEPS

Americo Giuliano Woolard

Abstract

The data rich nature of instrumented civil structures has brought attention to alternative applications outside of the traditional realm of structural health monitoring. An interest has been raised in using these vibration measurements for other applications such as human occupancy. An example of this is to use the vibrations measured from footsteps to locate occupants within a building. The localization of indoor footsteps can yield several benefits in areas such as security and threat detection, emergency response and evacuation, and building resource management, to name a few. The work described herein seeks to provide supplementary information to better define the problem of indoor footstep localization, and to investigate the use of several localization techniques in a *real-world*, operational building environment. The complexities of locating footsteps via indoor vibration measurements are discussed from a mechanics perspective using prior literature, and several techniques developed for localization in plate structures are considered for their applicability to indoor localization. A dispersion compensation tool is experimentally investigated for localization in an instrumented building. A machine learning approach is also explored using a nearest neighbor search. Additionally, a novel instrumentation method is designed based on a multi-point coupling approach that provides directional inference from a single point of measurement. This work contributes to solving the indoor footstep localization problem by consolidating the relevant mechanical knowledge and experimentally investigating several potential solutions.

SUPPLEMENTING LOCALIZATION ALGORITHMS FOR INDOOR FOOTSTEPS

Americo Giuliano Woolard

General Audience Abstract

Equipping buildings with sensors that can measure vibrations is a common way to keep track of the health of a building. This has brought attention to other ways of using the same technology. For example, the vibrations from footsteps may be used to track occupants inside of a building. Tracking occupants has many applications in areas such as security and threat detection, emergency response and evacuation, and building resource management, to name a few. The work described herein seeks to better understand the problem from a mechanical perspective, and to implement techniques designed more appropriately for localization in this type of environment. This work contributes to solving the indoor footstep localization problem by consolidating the relevant information and using experiments to investigate several potential solutions.

Per la mia famiglia che ha reso questo lavoro possibile
con il suo amore e support.

Acknowledgements

There are many people I would like to thank for their support throughout my time at Virginia Tech. I will do my best to express my thanks to those individuals, although it should be known that my gratitude extends beyond my vocabulary.

I would like to thank my advisor Dr. Pablo Tarazaga for providing an incredibly collaborative, supportive, and friendly environment. He has been an exemplary advisor and cares a great deal for his students.

My lab mates Austin Phoenix, Dustin Bales, Patrick Musgrave, and Rodrigo Sarlo have been the best colleagues I could ask for. Our countless discussions were always enjoyable. Mohammad Albakri, Bryan Joyce, and Sriram Malladi were all present when I joined the lab in 2013 and aided me numerous times in nearly every aspect of my academic progress. I cannot count how many questions I've asked these guys, and they were always happy to help. I also would like to thank Sriram ("Pancho") specifically, as he has been a great friend, and has gone above and beyond to help me on many occasions.

I must thank my good friend and roommate for several years Michael Jernigan. Mike and I have known each other for over 15 years. Our many discussions over that time have helped define me as a person, and it was he who introduced me to the engineering field.

I would also like to thank Lauren Fialkow for being there for me, even in the most difficult moments. Throughout our friendship she has enabled me to evolve as a person, and has shown me a level of compassion that was all but lost. I am a better person because of it. I must also acknowledge my friends Michael Koteski, Justin Lin, and Dylan Reingruber. While I have

been away at VT, my brief visits back home were always welcomed as if nothing had changed. Along with my family, these guys are what made Virginia Beach my home.

Finally, I would like to thank my family for their unwavering love and support. My brother Horace and sister Alba have always been supportive, and consistently expressed their faith and pride in my pursuit of a Ph.D. My father, Horace, and mother, Maria, have sacrificed so much for their children, and for that I am eternally grateful.

Table of Contents

List of Figures

List of Tables

Chapter 1 Introduction and Literature Review

1.1. Introduction

With the recent advent of "smart buildings" comes an invitation to test the capabilities and limits of these structures. What constitutes a "smart building" varies across disciplines, but generally it will have the quality of some type of automation that is coupled with a form of sensing and/or user interaction. The instrumentation of civil structures to measure vibrations is one form of sensing that has become more prevalent in recent years, often for applications related to structural health monitoring (SHM). While this is the primary appeal of vibration measurements within civil structures, the resulting data is rich in information and provides an opportunity to pursue novel research and its applications with these measurements. This research considers buildings instrumented to measure structural vibrations via accelerometers or geophones, and will focus on developing techniques that support localization of footsteps and other generalized impulsive events. Specifically, attention is drawn to the fundamental mechanics underlying indoor localization, the problems therein, and potential solutions. It is the purpose of this body of work to develop a better understanding of the mechanics of indoor footstep localization, and to investigate the implementation of several techniques in a real-world operational building environment. Traditional localization methods are discussed from analytical and practical perspectives, and compared with alternative methods designed specifically for localization in complex environments. Throughout this work, several localization techniques are implemented in both simulations and experiments. In addition, the pursuit of this work led to the realization of a novel instrumentation method that reduces the minimum number of sensors required for bearing

estimation. This method is formulated by exploiting the mechanics of the localization problem, and is investigated in a simulation environment.

1.2. Research Motivation

A system capable of accurately tracking occupants indoors introduces an assortment of benefits to society. One of these benefits is in emergency response and evacuation, where it is beneficial to first responders to know the location and number of occupants within a building. The majority of E911 calls come from indoor locations, which, in addition to public safety concerns, has prompted the FCC to issue new regulation regarding the localization of E911 callers. The new regulation requires service providers to be able to determine the location of E911 calls to within a 50 meter radius and a 3 meter vertical [1]. This is despite objections from both Verizon and T-Mobile that this accuracy would not be possible with current technologies. Providing emergency responders with accurate positioning information would have life-saving benefits for both the responders and the callers. Energy savings can also be achieved with an accurate indoor localization system. Having knowledge of where people are in a building allows for more efficient allocation of HVAC resources, which is estimated to consume about 39% of building energy [2]. While conventional occupancy sensors achieve a 5.9% reduction in energy costs, a more accurate positioning system is estimated to achieve an 18% reduction [3].

Although source localization is a well-developed topic, vibration based source localization is primarily a focus of seismology and damage detection. The interest in developing a localization method based on vibrations is founded on the shortcomings of more traditional approaches. In an indoor environment, locating occupants is still an area of active research due to some of the more

traditional techniques being insufficient. The most direct and obvious solutions such as cameras or computer vision could perform reliably, but suffer from privacy concerns both in general and due to advancements in facial recognition. Currently, one of the most prevalent localization methods is to use Global Positioning Systems (GPS). GPS works well in outdoor environments and often serves as the primary navigator for mobile devices, automobiles, etc., but struggles to perform well in indoor environments due to issues of signal attenuation and multipath created by the building structure. The use of GPS also requires that the occupant be equipped with a GPS capable device. Similarly, local wireless (WiFi) methods from carried devices can provide a more robust alternative [4]. Localization may also be achieved by equipping occupants with a Radio-Frequency Identification (RFID) chip [5]. Another method is the use of accelerometers or inertial measurement units on devices that are carried or worn ([6-9]). These approaches, however, all require occupants to intentionally be equipped with a device, which can be lost, forgotten, stolen, or intentionally not carried. User compliance is a major issue in all of these cases. If emergency evacuation responders rely on these technologies they could be lead to a location where a phone was left but no person is there (false positive). In the case of GPS or WiFi, the carried devices must also have the appropriate services enabled, which is often optional with cellular devices. Alternatively, there are several methods that do not require a device to be worn or carried. For example, RF can be used for localization based on body reflections [10], but can suffer from similar privacy concern issues as video and computer vision. A similar concern is present with using the acoustic signals from footsteps for localization [11], which requires microphones to be placed throughout the building. The use of pressure sensitive floors has also been investigated as another alternative [12, 13], but this technique can be both invasive and prohibitingly expensive.

Vibration based tracking provides an alternative approach, and is a well-suited addition to recent advancements in footstep detection. Detecting footsteps through seismic vibrations has been well researched, with many methods proving successful in a variety of environments [14-24]. Past studies show the Signal to Noise Ratio (SNR) of seismic signals generated by footsteps in outdoor urban environments as limiting the detection range to anywhere from 5 to 20 m depending on the rigidity of the walking style and other factors such as the walking surface [14, 25-27]. Some of these past experiments suggest the footstep signal must be around 6 dB or more above the noise floor for detection. In an indoor environment, we deal with a floor that is more akin to a plate than an elastic half-space, where elastic energy is restricted by the upper and lower traction-free boundaries of a plate. This suggests we can expect more energy to be retained throughout radial propagation and increase footstep detection range. Accelerometers placed on structural elements underneath a 7 in. thick concrete floor have been able to pick up footstep signals greater than 6 dB from 9 m away in a noisy construction environment [28].

In addition to detection, there is also a significant body of work in footstep classification and characterization that has been developed over the years [16, 29-37]. Many of these techniques exploit characteristics from the seismic signature of a footstep to perform tasks such as personnel identification or gender classification. Recent studies in gender classification have been particularly successful, achieving up to a 97% accuracy using machine learning techniques [38, 39]. With the potential to detect and classify footsteps, the ability to track individuals is a useful contribution, coupling well with the already rich information available. A vibration based tracking system has some of its own unique benefits, in addition to the described emergency response benefits and energy savings. Vibration based tracking can also allow for non-intrusive fall detection in hospitals or retirement communities, where quick response times can be life-saving

and privacy is a concern. Other realizable applications include determining the location of an abnormal event or tracking a moving threat that wants to stay hidden. More broadly, seeing how occupants move in a space discretely can provide valuable design consideration for architects, or provide retailers with a better understanding of consumer behavior, all while respecting privacy [40].

Instrumenting buildings or other civil structures to measure vibrations is not new [41-48]. While the primary purpose of this type of instrumentation is typically for seismic activity monitoring, SHM, or model validation, the hardware infrastructure required to measure footsteps is similar, providing an avenue for potential innovation. Expanding on the capabilities of indoor seismic measurements has been sought after in recent years to include cases such as occupancy estimation, indoor activity levels, and more recently, event localization [49-56]. In the past few years Virginia Tech has instrumented a new campus building – "Goodwin Hall" – to measure both structural vibrations as well as human activity [57]. Goodwin Hall is a 160,000-ft^2 building, with over 200 accelerometers structurally mounted throughout the building, and serves as the testing location for several of the experiments presented herein. The sensors were put in place during the construction of the building and comply with modern construction practices. Part of the instrumentation includes a densely-equipped corridor that provides an excellent platform to develop and test localization and tracking algorithms.

Vibration based localization in a building is a difficult task to accomplish due to effects such as dispersion, reflections, inhomogeneity, and material discontinuity. The purpose of this research is to provide physical insight to the problem in order to benefit the various localization and tracking techniques available. While localization in particular dispersive media has been accomplished in the past, the novelty of this research is in applying these techniques in a real-

world operational building environment, comparing them in a simplified environment, and developing a novel instrumentation method that aids in solving the localization problem. The following sections discuss in detail some of the past literature for footstep localization.

1.3. Overview of Footstep Localization through Vibrations

Previous literature has presented several techniques available for seismic source localization. These techniques can generally be categorized into three well-known methods: (1) amplitude attenuation over a distance (RSS in the wireless community), (2) arrival time differences, and (3) particle motion techniques. Amplitude attenuation methods use a distance based damping model to predict the "distance-difference" seen between sensors, providing a geometric relationship that is used to solve a set of nonlinear equations. Time-difference-of-arrival (TDOA) techniques rely on a similar positioning method, but instead of determining the distance-differences with relative signal decay, the time-difference is measured and scaled by an assumed (or known) wave speed. Chapter 2 discusses this type of localization in greater detail, as it is the most common form of localization. Lastly, particle motion techniques rely on the orthogonally relationship between longitudinal waves (P-waves) and transverse waves (S-waves), where the projection between the two can provide bearing estimates.

The applicability of these seismic source localization techniques for indoor footsteps are generally considered to be limited due to issues such as floor reflections, dispersion, and flexural mode dominance [52]. In outdoor environments, previous efforts to implement these methods have been found wanting, although TDOA techniques appear to be the most viable [58, 59]. Despite

these setbacks, seismic signals are still considered to be a promising avenue for personnel tracking [60], and more recent research efforts have proven to be successful in certain environments.

One recent method was implemented using a novel algorithm called the sign-of TDOA, or SO-TDOA [52]. This approach was developed in response to the poor-quality time-differences obtained from using traditional time-difference methods on a dispersive wave. The SO-TDOA uses only the order of arrival of the wave among the sensors, which is then mapped to a small area of the floor based on the geometry of the sensor positions. The experiment used nine floor-mounted accelerometers sampled at 20 kHz and determined that the SO-TDOA performed well in a small (3.6 m × 5.4 m) room, achieving localization to within 50 cm on average.

Due to the impact-like nature of footstep excitation, an interest has been taken in localizing indoor hammer strikes as a precursor to human localization due to its simplified input and more consistent repeatability. This was first shown in Goodwin Hall, where the sensors beneath the floor are structurally bonded to the supporting steel girders. Hammer strikes were located to within 230 *cm* using traditional TDOA with a sampling rate below 5 kHz, and an estimated wave speed of 914 *m/s* [55]. A similar experiment was conducted again using TDOA with a significantly higher sampling rate of 65 kHz [56]. Localization of hammer strikes achieved sub-meter accuracy, and preliminary results for footstep localization are shown but not reported. A further expansion of this work was done using a more sophisticated TDOA algorithm [53], where a sensor selection algorithm was incorporated based on SNR estimates. Detection was also implemented using a matched filter approach, which was also used to enhance the SNR of the measured signals. In addition, wave speeds were incorporated into the localization problem. The results showed an increase in localization accuracy of hammer strikes to within 0.5 m. The methods for enhancing the localization of hammer strikes in [53] were later applied to footstep localization [61]. The

sampling rate was reduced to 32 kHz, and several additions were made to the TDOA localization algorithm. First, the matched filters were expanded to also include detection of when a footstep occurs directly above one of the sensors, as this was found to produce a unique time-series. Second, Akaike Information Criterion [62] was incorporated to enhance the accuracy of the estimated arrival times. This significantly more sophisticated approach resulted in sub meter accuracy for footstep localization in two separate areas of the instrumented building. Another method developed in a different building used 3 on-floor geophones to locate footsteps [63]. The measured signals were decomposed using wavelet decomposition [64], and the wavelet with the highest energy is used for localization. A set of trial footsteps from an individual was used to estimate the effective wave velocity of the decomposed signal. This method achieved a footstep localization to within 0.5 m.

While many of these methods have been shown to be functional, their application has been limited to environments with relatively dense sensor networks. One of the major factors of this is due to difficulties in predicting the wave behavior over long distances in a complex building environment. The problem is further exacerbated by the issue of dispersion, causing the waveform to distort as it propagates. The structural variations throughout a building structure lead to additional complications in the measured signal by providing a medium with inconsistent dispersion properties. In addition, the attempts made at footstep localization were for a single occupant, and since many of the techniques require some optimization they may be more difficult to implement for multiple occupants.

1.4. Dissertation Outline

This section describes the organization of the thesis. In Chapter 2, a brief discussion on the fundamentals of localization are provided, along with its context in localizing source-emissions in elastic media. This is then extended to a simplified floor, and the affects of various aspects of the media are considered. The resulting formulation of the wave dynamics leads to the assimilation of a building floor to a thin plate, and discusses techniques that have been developed for this type of environment. Chapter 3 investigates the difficulties of implementing the localization problem on a thin plate when using traditional TDOA techniques. The effects of reflections are also investigated, along with the applicability of the SO-TDOA algorithm. In Chapter 4, impacts are located in Goodwin Hall using techniques designed for plate localization. The results are compared with traditional TDOA methods. In Chapter 5, a machine learning approach is investigated as a way to locate various impacts and footsteps in an indoor building. In Chapter 6, a novel instrumentation method is implemented in a simulation environment to investigate the potential of single-sensor bearing estimation. Conclusions are provided in Chapter 6, along with potential avenues for future work.

1.5. Contributions

This dissertation makes progress towards the indoor localization of occupants through floor vibrations. The problems associated with indoor localization are outlined, and insight is provided into potential solutions while investigating some of the less traditional techniques that can be applied in such a complex environment. A comprehensive overview of the indoor localization

problem is provided, which highlights the issues associated with traditional localization techniques. The difficulties are structured such that the qualities of an accurate indoor localization system can be well defined. Prior research in this field tends to seek methods that alleviate the difficulties associated with indoor localization, as opposed to incorporating them into the problem. The comprehensive review highlights these difficulties and suggests several solutions that follow from the fundamentals of localization theory. Several of these potential solutions which have not been used for indoor localization are implemented in both simulation and experimental environments. The conclusions drawn from this work better define the localization problem and equip future researchers to implement novel methods for indoor footstep localization.

Chapter 2 Problem Formulation

2.1. Introduction

Appreciating the underlying mechanics of indoor footstep localization provides a direct avenue to incorporate models that enhance overall accuracy. Localization is an expansive topic with a wide variety of solutions for a myriad of applications. To make the information available more manageable, interests herein are limited to localization in 2-D space, where emissions occur at an unknown time. Discussing only this scenario helps isolate what is most applicable for passive footstep localization. The methodology for multidimensional, source-emission based localization relies fundamentally on the pursuit of maximum-likelihood solutions to a set (or subset) of nonlinear equations. To develop the context of indoor localization, an overview of the most prevalent positioning method is first discussed to provide a basis for what follows. Then, a brief introduction to the governing equations for waves propagating in a plate is provided. Footstep loading is also considered using past literature, and is incorporated into the analytics of wave propagation. Considering footstep dynamics shows how the behavior of a building floor can be simplified to a thin plate under certain assumptions. The developed understanding leads to a holistic vantage point from where the localization problem and its potential solutions can be discussed.

The discussion that follows is separated into several parts. First, the floor is considered as an isotropic and homogeneous plate. Plate theory is well suited to describe the waves propagating in this environment. Second, the effects of various concrete elements are considered, such as the

supporting steel deck, concrete reinforcements, and the variability of the aggregate. Third, the structural members are discussed, along with the non-structural partitions within the building. Lastly, several methods of performing localization in these types of environments are considered for their applicability in a complex building environment.

2.2. Localization

The two-dimensional localization problem is defined here as follows. For an emissive source, the distance d_i to the i^{th} receiver is described using Cartesian coordinates as

$$d_i = \sqrt{(x_i - x_0)^2 + (y_i - y_0)^2}, \tag{2.1}$$

where x_i, y_i are the known coordinates of each of N total sensors, and x_0, y_0 are the unknown coordinates of the source. This is illustrated in Figure 2.1. If the propagation speed for the emission from the source is assumed to be constant, then the distance from the source to the sensor is taken to be based on the travel time for the emission to reach the sensor, i.e.,

$$d_i = c(t_i - t_0), \tag{2.2}$$

where c is the assumed constant wave velocity, t_i is the arrival time of the emission, and t_0 is the initial time that the emission occurred. It is often the case that t_0 is unknown, and t_i can be estimated. Putting Eq. (2.1) and Eq. (2.2) together yields

$$c(t_i - t_0) = \sqrt{(x_i - x_0)^2 + (y_i - y_0)^2}, \text{ for } i = 1{:}N \tag{2.3}$$

with unknowns t_0, x_0, and y_0. At least $N = 3$ sensors are needed to solve for the 3 unknown variables.

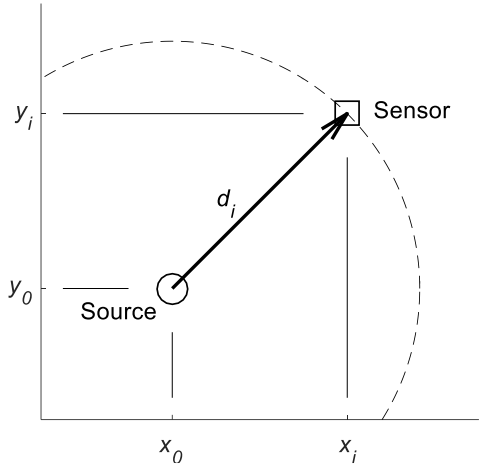

Figure 2.1. Illustration of the distance separating an emissive source to a sensor.

Using Eq. (3) in this form is known as the time-of-arrival (TOA) problem. TOA solves for the unknown variables by minimizing a predefined error function. It is important to note that an accurate t_i is not exactly necessary, but that the difference between t_i and t_0 be consistent (since t_i is added with t_0, a consistent shift in the estimated $t_i$will proportionally the value of t_0 which minimizes the error). An alternative formulation reduces the number of equations and unknowns by subtracting the distance from a reference sensor, i.e., with $d_{1i} \equiv d_1 - d_i$, and $t_{1i} \equiv t_1 - t_i$,

$$ct_{1i} = \sqrt{(x_1 - x_0)^2 + (y_1 - y_0)^2} - \sqrt{(x_i - x_0)^2 + (y_i - y_0)^2}. \tag{2.4}$$

The formulation in Eq. (4) is known as time-difference-of-arrival (TDOA) [65], and is common in the acoustics and wireless fields. This is referred to herein as TDOA, although other names, such as Inter-aural-time-difference (ITD) or inter-aural-phase-difference (IPD) are alternatives for the same concept [66]. TDOA provides $N-1$ equations while removing the need to solve for t_0. At least $N=3$ sensors are needed to produce 2 unique equations to solve for x_0 and y_0. Eqs. (2.3) and (2.4) are nonlinear, and the solution can be found using one of many nonlinear solvers. For example, the Levenberg-Marquardt [67] or the Chan and Ho [68] algorithms are popular choices for solving the more common TDOA representation. The methods of solving these equations is well established in the literature, and can be found in many of the provided references that implement localization.

The ct_{1i} term can be referred to as the "distance-difference." As a conceptual example, if a line is drawn from each of two sensors to the source, their difference in length is the distance-difference. The solution to each of the $N-1$ equations represented by Eq. (2.4) lies on a hyperbolic line that corresponds to the location requirements that would produce the same distance-difference seen by the sensors. The intersection of these lines corresponds to the source's location. For each sensor pair, the corresponding hyperbola has an apex that orthogonally intersects the centerline of the sensor pair, and the focus of the hyperbola is located at the sensor that received the signal first. An example of this is shown in Figure 2.2a, where 3 sensors are used to produce 2 intersecting hyperbolae. The distance-differences are formulated using the first sensor as a reference and scaling the time-of-arrival differences by a constant wave speed. Using more than three sensors over-determines the system and produces more than one intersection point. In the ideal environment, all the intersection points for an over-determined system would be the same, however, with the presence of noise, this is not the case.

An example of this is shown in Figure 2.2b. The problem then becomes a question of picking the location that disagrees least with the spatial requirements (e.g., [68]).

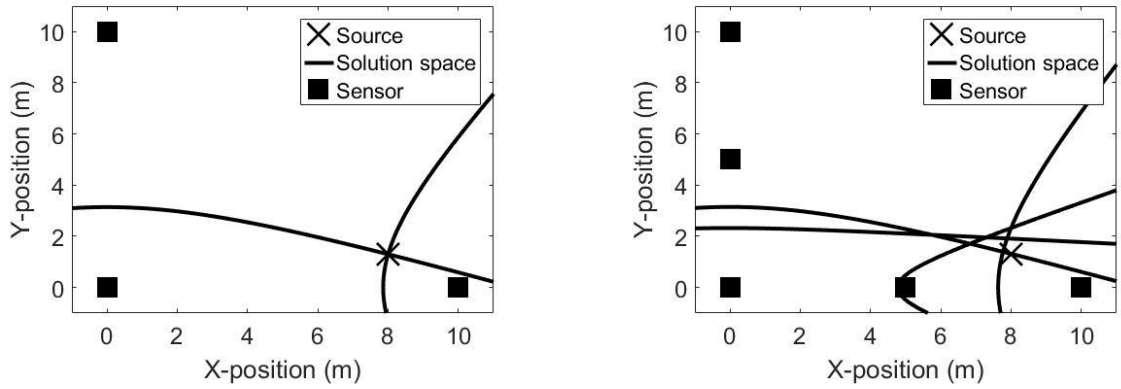

(a) (b)

Figure 2.2. (a) **Example of localization in an ideal environment using 3 sensors to produce 2 hyperbolae, and (b) in a noisy environment using multiple sensors.**

The time differences can be calculated in several ways. Two common methods which are implemented in a later study are to use either peak-detection or cross-correlation. The peak-detection method uses the difference in time of maximum amplitude of the signals, i.e., for a measured time-trace $y_i(t)$ at the i^{th} sensor

$$t_i = \arg\max_t \big(y_i(t)\big). \tag{2.5}$$

With the cross-correlation method the two signals are convolved, with one being time-reversed, and the time-difference is taken as the lag-time of maximum correlation [69]. This can be shown as

$$t_{1i} = \arg\max_\tau \Big(\int_{-\infty}^{\infty} y_1(t) y_i(t-\tau)\ d\tau\Big). \tag{2.6}$$

Much of the current work in vibration based footstep localization focuses on using TDOA. Implementing TDOA requires accurately calculating the difference in arrival time of an emission between several sensors and in the form of Eq. (2.4) requires the assumption that the resulting emission from excitation propagates as a waveform at a constant velocity. This is often not the case in bounded media (like a building floor), where dispersion arises and the wave speed is frequency dependent. This will be discussed in further detail in the next section.

2.2. Wave Propagation in a Simplified Building Floor

The emitted wave that results from a footstep is a product of the building floor characteristics. While there are many different types of building floors (e.g., [70]), the focus here is limited to composite steel floors, although the concepts are generally applicable to all floor types. An example of a typical composite steel floor is shown in Figure 2.3a. The floor consists of concrete poured over a steel deck, which is supported by the steel structural members within the building. A typical layout of a full floor within the building is shown in Figure 2.3b, where the concrete slab and steel deck assembly is supported by a grid of steel girders and several columns. Along the surface of the full floor can exist many non-structural elements (e.g., partitions, furniture) that can affect the dynamic behavior of the floor as well. Some buildings may also have an access floor, which is a small space that exists beneath the steel deck and is used to house things such as wiring, piping, etc.

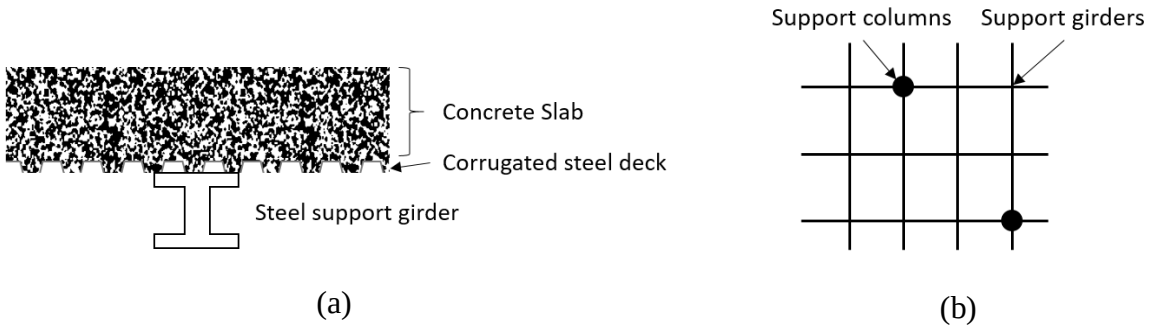

Figure 2.3. A sketch of the layup for a typical composite steel floor (a), and an example of a floor section as seen from above (b), over which concrete is poured.

To simplify the dynamics of this structure initially, the entire concrete floor is treated as a homogenous plate, with the corrugated deck and I-beams neglected. By this way, we can focus on wave propagations in an elastic plate to get a first impression of the floor response to footsteps. Since footstep loading is primarily in the vertical direction [71], attention is focused only on the shear-vertical (SV) and pressure (P) waves, effectively assuming a plane strain condition where the displacement vector is radially symmetric. A more in depth discussion on the ground reaction forces of footsteps is discussed later in this chapter and its implications are considered. Under the plain strain consideration, only the cross section of the plate is needed for analysis, shown in Figure 2.4. The equations used here are a simplified outline of those found in [72].

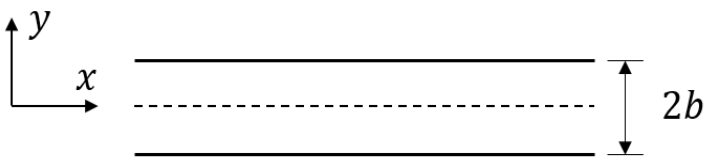

Figure 2.4. Simplified analytical model equating a building floor to a homogeneous, isotropic plate.

The governing equations for a homogeneous, isotropic solid can be stated in their most comprehensive form by using the scalar and vector potentials Φ and $\mathbf{H}$, such that the displacement vector

$$\mathbf{u} = \nabla\Phi + \nabla \times \mathbf{H}, \quad \nabla \cdot \mathbf{H} = 0. \tag{2.7}$$

Some reductions can be applied for the case of a homogenous plate. The plane strain assumption ignores the shear-horizontal (SH) components and assumes $u_z = \partial/\partial_z = 0$, which neglects displacement variation in the z-direction and prohibits the existence of Love waves (SH). This reduces the governing equations (albeit in a less compact form) to

$$u_x = \frac{\partial\Phi}{\partial x} + \frac{\partial H_z}{\partial y}, \; u_y = \frac{\partial\Phi}{\partial y} - \frac{\partial H_z}{\partial x}, \tag{2.8}$$

$$\nabla^2\Phi = \frac{1}{c_l^2}\frac{\partial^2\Phi}{\partial t^2}, \qquad \nabla^2 H_z = \frac{1}{c_s^2}\frac{\partial^2 H_z}{\partial t^2}, \tag{2.9}$$

where the c_l and c_s terms are the longitudinal and shear wave velocities in bulk media. Under this plane strain consideration of the governing equations, the traction-free boundary conditions are applied such that

$$u_y = \tau_{xy} = \tau_{zy} = 0, \qquad y = \pm b, \tag{2.10}$$

where τ is the stress tensor. The solution to these equations yields the dispersion relation, which defines the relationship between frequency and wavenumber for a propagating wave. From this point, solving the generalized wave equation for radially symmetric waves and some non-trivial manipulation yields two Rayleigh-Lamb frequency equations, which are combined to form a more general single equation given by

$$\frac{\tan \beta b}{\tan \alpha b} = \left(\frac{4\alpha\beta\xi^2}{(\xi^2-\beta^2)^2}\right)^{\pm 1} = 0 \quad \begin{cases} +1 = symmetric \\ -1 = antisymmetric \end{cases}, \tag{2.11}$$

with

$$(\alpha, \beta)^2 \equiv \frac{\omega^2}{c_{l,s}^2} - \xi^2 \ , \tag{2.12}$$

where ω and k are the radial frequency and wavenumber, and b is half of the plate-thickness. The solution to Eq. (2.11) introduces a group of radially symmetric waves referred to as Rayleigh-Lamb waves, or just "Lamb" waves. It is evident from the equations that this relationship is nonlinear, which leads to a frequency dependent propagation velocity and a difference between the phase and group velocities. There exist two dominant wave modes for Lamb waves corresponding to either the symmetric or antisymmetric case. The P-waves are in-plane waves and are symmetric about the centerline of the plate. The particles move in the direction of propagation, and an effective "bulging" occurs about the centerline. The SV-waves have out-of-plane particle motion, and are anti-symmetric about the centerline. Figure 2.5 shows a sketch of the displacement for both cases. For each of these wave modes there exists infinite higher-order modes, each with a nascent frequency, below which the wavenumber is resolved as imaginary and the wave mode does not exist. Figure 2.6 shows an example of these dispersion modes and their higher orders. The first antisymmetric and symmetric modes are labeled A0 and S0, respectively. These fundamental modes do not have a nascent frequency and exist over the entire frequency range. Since impacts on a plate predominantly excite in the vertical direction, and are dominated by low frequency energy, it is a safe assumption that much of the energy in the propagating wave will

exist within the A0 mode [52, 73, 74]. The assumptions for footstep forces are briefly investigated in the following section, where the dynamic loading of footsteps is discussed.

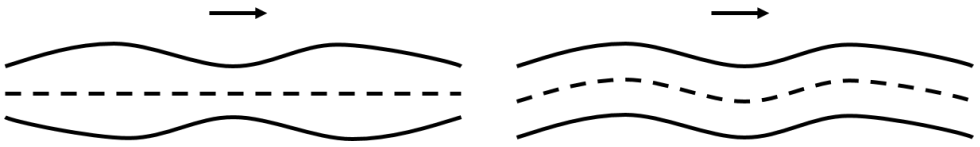

Figure 2.5. Sketch of the symmetric (left) and antisymmetric (right) Lamb wave modes.

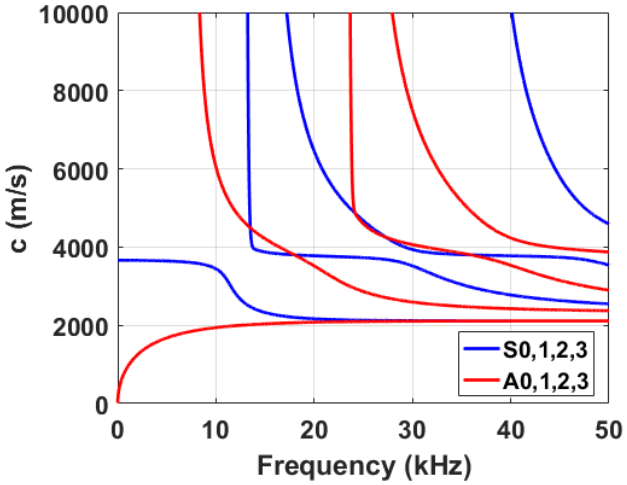

Figure 2.6. Example of the dispersion relation for Lamb waves in a plate. Symmetric (blue) and antisymmetric (red) wave modes are shown for the fundamental modes (S0, A0) and higher orders.

2.3. Footstep Reaction Forces

The ground reaction force of a footstep is broken into three orthogonal force components: vertical, antero-postmerior, and medial lateral. The vertical component is normal to the ground surface, or “up and down” from the walker’s perspective. The antero-posterior component is in the direction of walking, or “forward and backwards”. The medial-lateral component is orthogonal to

the walking direction, i.e. “left and right”. Much of the work done for characterizing the ground reaction force to footsteps is with regards to either biomedical research or gait analysis for human-structure interactions (HSI). For the latter, it is typical for the walking frequency (i.e., the rate in which footsteps occur) to be of importance, as this can contribute significantly to ground motion in civil structures. The problem of footstep localization is not concerned with the walking frequency, but only in the frequency bandwidth excited by a single footstep with which to characterize the propagating wave. In high-frequency (rigid) floors, the response from a footstep decays quite rapidly, thus the dynamics resulting from prior footsteps will not significantly affect the measured response of the current footstep. It is important to note, however, that walking frequencies typically range between 1.5 to 2.5 Hz [75], thus it would be ideal for a localization algorithm intent on tracking to function within the timeframe allotted between footsteps, or about 0.5 s. For low-frequency floors, the lower modes of vibration can persist well beyond the initial footstep, and possibly lead to resonance [76, 77], which is a major concern in HSI. In this type of environment, it may be necessary to filter out the excited floor modes.

Past studies of footstep localization indoors have found using only the vertical component of excitation as sufficient for modeling wave propagations in a building floor [52]. In fact, several studies have shown that the vertical component of footstep excitation has a magnitude of 0.5 to 1.25 times the body weight (BW) [78], compared to the medial-lateral or anterior-posterior components, which are closer to 0.15 times the BW [79, 80]. This suggests that, for localization applications, the vertical component of excitation will govern the majority of the response.

Regardless of the floor type, the bandwidth of excitation from the vertical component of a single footstep is typically in the range of 10 to 100 Hz [79-81]. An example of the vertical loading from a typical footstep is shown in Figure 2.7.

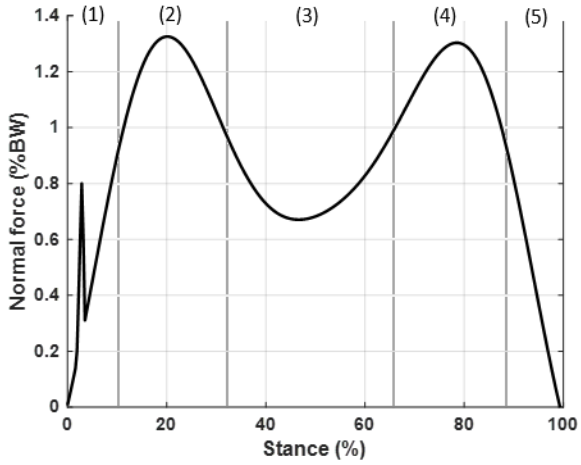

Figure 2.7. Example of the vertical ground loading of a footstep. The transient is broken into sections (1) through (5) corresponding to the typical loading phases of a footstep.

The function used [76] is:

$$F(t) = L(1 + \sum_{k=1}^{K} b_k \sin(k\omega_0 t + \phi_k)) \tag{2.13}$$

where L is the static weight of the walker, b_k and ϕ_k are the Fourier coefficient and phase shift of the k^{th} harmonic, K is the total number of significant harmonics, and ω_0 is the walking frequency.

The typical footstep will follow five phases: (1) the heel of the foot makes initial contact with the ground; (2) the weight is settled on the heel of the foot; (3) the weight is on the middle of the foot, transitioning from the heel to the ball; (4) the weight is on the ball of the foot; and (5) the toes of the foot separate from the ground. The different stages of the footstep can be seen in Figure 2.5. The initial spike in the data during the first phase of the footstep cycle belongs to the first contact made with the heel of the foot, often referred to as a "heel-strike". Eq. (5) does not include this initial spike as it is often neglected in HSI due to the small importance of the higher frequency

content, and so it has been artificially added. The heel-strike of a footstep is the most broadband component of excitation, usually lasting for 10-20 ms with energy in the 10 to 75 Hz bandwidth, and a peak force of 0.5-2.25 times the body weight [79, 82].

The friction force between a foot and the floor can produce high-frequency vibrations as well, with content in the range of 10-15 kHz. A previous study that measured the frictional forces from footsteps showed a large portion of the energy below 500 Hz, and another, nearly equal amplitude spike in the 10-20 kHz range [25]. The same study compared walking styles as well, which were categorized as being either regular, soft, or stealthy. All of these walking styles had similar characteristic bandwidths, separated primarily by the magnitude of the response. Similarly, looking at the vertical component of high-heel forces on various surfaces (linoleum, bare concrete, and hardwood) had the majority of content below 500 Hz, while surfaces like carpet or woven fiber rugs had most content below 125 Hz [83]. Walking and running appear to have similar frequency content as walking, with the main differences being in peak force increases of up to 2.45 BW [84]. The main difference with running, however, is that the waveform tends to change shape, with the two peaks shown initially for walking (see Figure 2.5) moving closer together, and at higher running speeds will merge into one dominant peak [70, 79].

In summary, the forces from footstep excitation are predominantly in the vertical direction, and confined within the 10-100 Hz bandwidth. Harder shoes can increase the frequency spread of this content, with high-heels exciting up to 500 Hz. Walking, jogging, or running, all produce similar trends in frequency content as walking but with greater force magnitudes. The in-plane forces, while comparatively low in amplitude, can provide significantly higher bandwidths, with the friction excitation reaching up to 20 kHz. It is no doubt then that in environments with sufficiently large SNR, the less dispersive in-plane waves excited from frictional forces may be

better suited for localization. However, in practice, the SNR in a build environment is likely insufficient to measure these in-plane forces. The next section discusses this in more detail, along with the response of a building floor under footstep excitation.

2.4. Reduction to thin plates

Assuming the loading dynamics described for a footstep in section 2.4 are representative, the dispersion relation from Eq. (2.11) for a plate can be reduced. When the wavelength of a propagating shear wave is long relative to the plate thickness, then the plate dynamics may be well described by a thin plate model. Likewise, when the wavelength is short relative to the plate thickness, the dynamics reduce to that of an elastic half-space, and the dynamics are governed by surface waves. In-between the two extremes, the various modes of Lamb waves dominate propagation.

In the case of a footstep, the low frequency of excitation leads to wavelengths that are much larger than the plate thickness. When the thickness of the plate is low compared to the wavelength, i.e.:

$$\alpha, \beta \ll \frac{2\pi}{b}, \tag{2.14}$$

then Eq. (2.11) reduces to:

$$c_p = \xi b \left(\frac{E}{3\rho(1-\nu^2)}\right)^{\frac{1}{2}}, \tag{2.15}$$

where the phase velocity c_p is linearly dependent on the wavenumber k. This equation is easily recognized as the flexural wave mode from thin plate theory. To put this in perspective, consider an 18 cm (7 in.) thick concrete slab. For properties, we will use estimates provided by the

construction company that built Virginia Tech's instrumented building: Goodwin Hall ($E =$ 31.5 GPa, $\rho = 2443$ kg/m^3, $\nu =$ 0.2). The dispersion relation for Eq. (2.11) and Eq. (2.15) are shown in Figure 2.8. Figure 2.8a uses the non-dimensional wave speed $\bar{c} \equiv c_p/c_2$ for comparison. The thin plate representation is shown to be accurate for a concrete slab of the prescribed properties up to about 400 Hz. This suggests that the low frequency vibration waves produced from footsteps can be well explained with the flexural wave mode of a thin plate provided an isotropic, homogenous medium. An exception may exist for impacts similar to the heel strike, where the content can excite up to 500 Hz. More importantly, however, is that we are well below the nascent frequency of the A1 wave mode (about 8 kHz, see Figure 2.6). In fact, the model used in [52] for the perceived propagation velocity of footsteps on a concrete floor have matched well with those obtained using only the flexural wave component from thin plate theory.

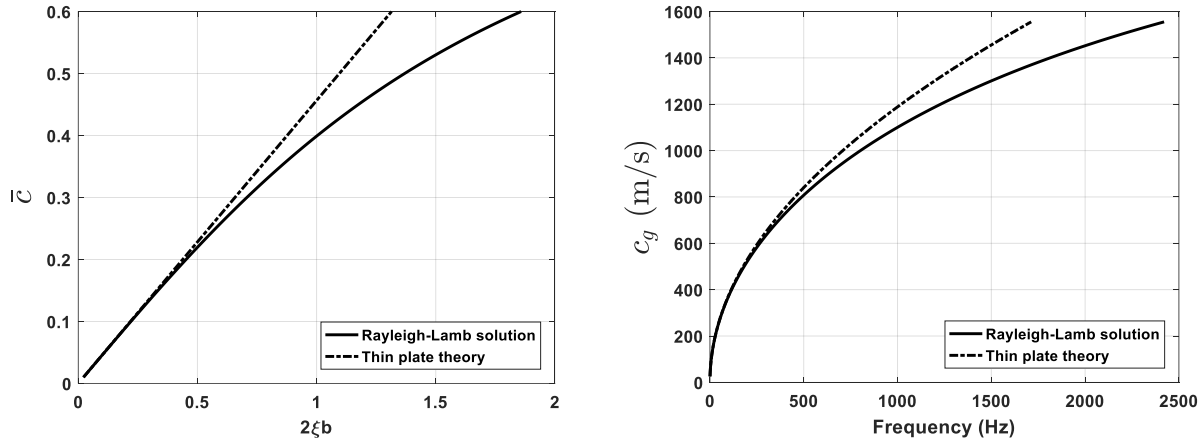

Figure 2.8. Comparison of the A0 wave mode between the numerical solution for the Rayleigh-Lamb equation and the thin-plate approximation.

2.5. Effects of Dispersion on TDOA Localization

In dispersive media, time-difference methods are more difficult to implement than in non-dispersive media. In non-dispersive media, a constant propagation velocity is used. For dispersive media, the propagation velocity is frequency dependent, and thus the arrival time-differences are frequency dependent.

Consider a 2-cycle tone burst propagating in an aluminum beam with no damping or noise. Figure 2.9 shows the waveform after it has propagated one meter and is compared against what it would look like in a non-dispersive medium. The non-dispersive case uses the shear wave speed in aluminum as a constant phase velocity, while the dispersive case uses the dispersion model derived from Timoshenko beam theory for a flexural wave. In the non-dispersive case, the propagated wave retains both the phase and amplitude characteristics of the original signal with only a time shift. In this case, the wavenumber is linearly dependent on the frequency, and thus the phase and group velocities are the same, yielding a signal which does not distort as it travels. For the dispersive case, the wavenumber is not linearly dependent on frequency, and so the group velocity is much faster than the phase velocity. Take for example the case of a thin plate, where Eq. 2.15 may be rewritten

$$c_p \equiv \frac{\omega}{k} = \alpha k, \qquad \omega = \alpha k^2 \,, \tag{2.16}$$

where α retains the plate properties. This is readily recognized as the dispersion relation from Euler-Bernoulli beam theory. It is evident now for the group velocity to be

$$c_g \equiv \frac{\partial \omega}{\partial k} = 2\alpha k \,, \tag{2.17}$$

which is exactly twice the phase velocity. In other words, the energy of the wave propagates at twice the speed of any individual peak. Practically, this means that as the peaks propagate, new peaks are formed in the front of the wave, while the peaks in the back become smaller. This can make both peak-detection and cross-correlation techniques used for calculating arrival time differences difficult to implement.

Consider a wave that has been measured at several distances from the source shown in Figure 2.10. If this were a non-dispersive medium, the velocity could be measured over one distance and extrapolated to greater distances. In a dispersive environment, this is not the case, because the wave speed is not constant, and appears to be different when measured from different distances. Using the measurement at 0.5 m as a reference, the cross-correlation method is used to calculate the TDOAs as 1.9 ms, 4.8 ms, and 13.3 ms, respectively. Dividing the TDOAs by the known distances yields speeds of 260, 314, and 337 m/s. For reference, the phase velocity of the center frequency is about 380 m/s. Using the peak-detection method in this scenario yields nearly identical results. The distance dependence on the measured velocity is the reason why time-difference methods are difficult to implement in dispersive environments.

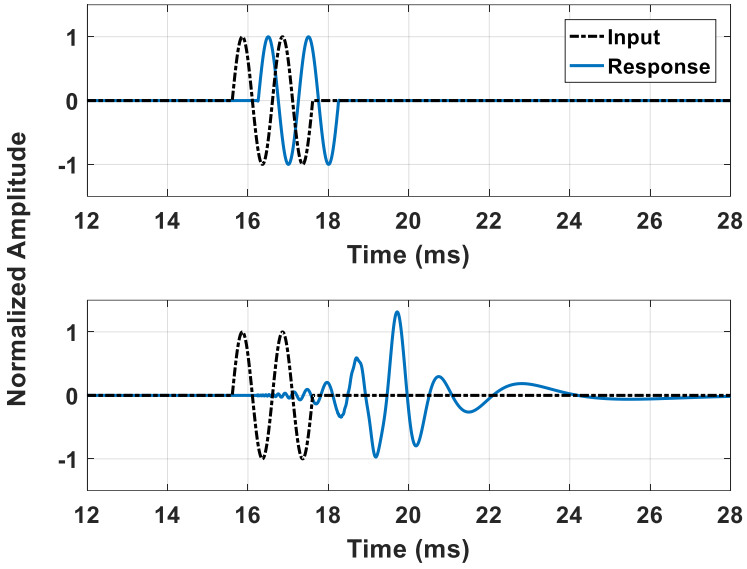

Figure 2.9. Wave propagating in an aluminum beam for the non-dispersive (top) and dispersive (bottom) case. The non-dispersive case assumes the bulk shear wave speed for aluminum.

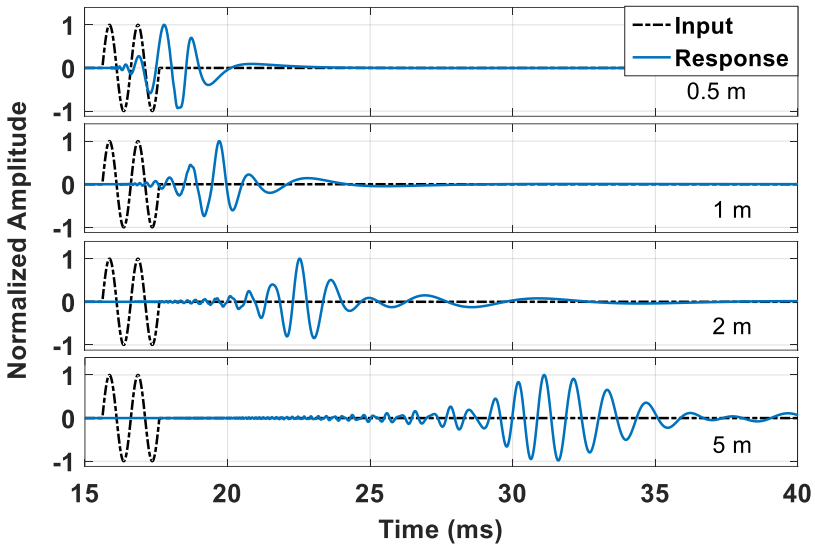

Figure 2.10. Dispersive waves propagating in an aluminum beam measured at 0.5, 1, 2, and 5m from the excitation point.

2.6. Effects of additional building elements

This section discusses in greater detail the effects of various components of a typical composite steel building floor. The inhomogeneous nature of concrete is considered along with the effects of various structural and non-structural elements.

2.6.1. Effects of concrete variability

Under the homogenous assumption, the effects of the steel deck are ignored, along with those that result from the inhomogeneous nature of concrete (e.g., various particles sizes, rebar, cavities, and defects). There is a lack of literature available on the lamb wave characteristics in a building floor. Therefore, in order to qualify the effects of these features, previous literature on damage detection in solid structures is observed. In damage detection, the ability to detect defects in a structure is dependent on the wavelength of the source relative to both the size of the defect and the stiffness change due to the defect [85-88]. While there is no established rule for this, small defects less than a one-tenth of the wavelength are often considered negligible. This is well described by the nature of elastic waves. The speed of the shear wave velocity in bulk media is

$$c_2 = \sqrt{\mu/\rho}\,, \tag{2.18}$$

with the wave speed being dependent on the shear modulus (μ) and density (ρ) of the material. The frequency content of a wave as it meets another media remains constant, although there is an impedance shift (i.e., $\rho_1 c_1 \rightarrow \rho_2 c_2$) as it enters the new media. If, over the wavelength, the change in impedance caused by the defect is negligibly small, then the wave will be purely transmitted

(i.e., impedance matching). This will occur if either the effect of the defect is very small compared to the wavelength, or when the wave speed along the defect is the same as in the waveguide. If the interface is completely rigid (fixed boundary), or the interface is a complete discontinuity (free boundary), then the wave is purely reflected. The exact ratio of transmission and reflection depends on many factors. More information on this can be found elsewhere (e.g., [72]) for simple media.

To put this into perspective, consider a sinusoidal wave propagating at 100 Hz in a building floor. Using the previous estimates for concrete properties, the thin-plate model yields a wavelength of over 3 m long. Not only would the various particle defects and (small) cracks be undetectable in this frequency range, but even large diameter rebar (about 60 mm) would yield very little if any reflections or distortion of the waveform. The same is true of the various particle defects and small cracks. Large cracks, however, could lower the stiffness significantly and effect a larger portion of the wavelength, which can result in wave distortion and reflection.

2.6.2. Effects of structural members

The additional contributions to wave dynamics from structural members is discussed from the steady-state perspective in HSI. A common practice for modeling the behavior of floors under human excitation is to consider the entire floor section, including structural supporting members, as all components of a stiffened isotropic plate [77, 89-91]. This is often the case for low frequency excitations, which will usually provide the greatest amplitudes, and are of greatest concern for HSI. Higher frequency excitations, however, have been shown to reveal higher-order modes, where the local bays vibrate out of phase [92]. From the wave propagation perspective, this suggests that a portion of the energy from footstep excitation is transmitted across the structural

boundaries of a local bay, while the rest is retained within the bay. The implications of this for localization is that a sensor located on the floor would measure reflections from not only the boundaries of the entire floor, but also from the local bays, and anything measured after the first arrival of the wave will contain low frequency modes. Additionally, the higher frequency waves must behave differently when the footstep occurs directly on the support, as these locations behave as nodal lines for the higher order modes.

The only locations of pure reflection on a building floor would be any finite boundaries of the floor itself. The small width of the structural supports relative to the length of the wave suggest that at worst there would be significant reflections, but transmission still occurs across these boundaries. This is also the case with the vertical support columns within the building. It may be intuitive to assume the column supports provide an interface sufficiently rigid for pure reflection, however, this has been shown in the past to not be the case [90]. The mode shapes at low frequencies show deflections at these locations. It is unlikely, then, in this case, that the bandwidth from footstep excitation would be purely reflected, but instead would both transmit and reflect portions of the signal similar to the effects of the structural girders.

Localization in this type of heavy reflection environment can be difficult to implement without prior knowledge of the media. The problem of reflections is one found often in many areas of localization. In these environments, the problem can be overcome by modeling of the reflections and using statistical approaches.

2.6.3. Effects of non-structural members

While the effects of non-structural members are often assumed to be negligible, they have been found to have significant impact on floor vibration modes in certain environments [70, 89, 90, 93]. Past research has shown that these effects can be profound in either increasing or decreasing the natural frequency of the floor. The extent of which is dependent on the mode shape and relative orientation of the non-structural members, along with the mass and stiffness contributions of each. In the context of guided waves, this can result in shifting the apparent wave speed to be higher or lower than it would be in the slab itself, much like the effects of structural girders, but to a (likely) lesser extent. Past research has shown over a 150% increase in the natural frequency of a large concrete slab after the addition of several full height partitions, and up to 5% for half-height partitions [70]. In this extreme example, the wave speed can be significantly increased in this area (and thus the wavenumber decreases), which is important to consider for localization purposes. Access floors can also affect the natural frequency of building floors. Similar to the effects of half-height partitions, the natural frequency has been shown to either increase or decrease depending on both the structure and orientation of the access flooring [93].

Non-structural members, particularly full-height partitions, can significantly affect the stiffness to mass ratio seen by the propagating waves. As would be expected, the orientation, total mass, and structure of the non-structural element determines its effects on the propagating wave. This further increases the amount of asymmetry that exists in the building, and can make it quite difficult to accurately predict the dispersion characteristics from one point to another.

2.7. Localization in plates

If the plate model is accepted as a decent representation of a building floor, then various plate

localization methods can be considered. There are many different techniques available in the literature, some of which are only applicable for isotropic, homogenous structures. The various plate localization methods are loosely categorized here as either (1) model-based, (2) partially model-based, or (3) do not use a model.

Model-based approaches require the dynamics of the structure to be known ahead of time, and can neglect the localization problem represented in Eq. (2.3) and Eq. (2.4) entirely. Models can be developed to find the transfer function of the plate, regardless of its geometry. This can be implemented using both finite-element models for more complicated structures, or analytical models for isotropic, homogenous plates [94-96]. Alternatively, experimental data may be used to develop the transfer functions [97-99]. When the transfer function of the plate is defined, the source location can be determined by the unique response produced at the (appropriately placed) sensors. Another approach placed in this category is to use machine learning or a comparison method to determine the most similar candidate from the database of impulse responses. This has been done using both simulations to create the model used for comparisons [100], or (more commonly) through experimental data [101-106]. All of these methods require the response of the structure to be well defined prior to localization, which requires extensive testing in a complex building environment. However, these methods have the benefit of functioning regardless of the complexity of the structure, since the behavior of the structure is established prior to localization, and there are no assumptions on isotropy or homogeneity.

Partially model-based approaches consider only a portion of the structural dynamics, which are then incorporated into the localization problem. As previously mentioned, the wave speed is frequency dependent and propagates at the group velocity. Equation (2.4) becomes:

$$c_g(\omega)t_{1i} = \sqrt{(x_1 - x_0)^2 + (y_1 - y_0)^2} - \sqrt{(x_i - x_0)^2 + (y_i - y_0)^2}. \quad (2.19)$$

Similar to Eq. (2.4), assuming the group velocity is known allows the solution to be resolvable with $N = 3$ sensors. Since the group velocity is frequency dependent, this can be done for either a single frequency, or for the entire bandwidth of interest. Obtaining the group velocity for a single frequency component has been done using a filter [74], or, more recently, using the Continuous Wavelet Transform (CWT) [107] by taking the wavelet with the highest energy [108]. If the dispersion relation is known ahead of time, (through either experiments or a developed model), the adverse effects can be compensated for using one of several dispersion compensation techniques (e.g., [109-113]). Implementing dispersion compensation for plate localization has been done in several studies experimentally [73, 113, 114]. In material that is not isotropic, the group velocity becomes dependent on the angle of propagation as well, i.e. $c_g(\omega, \theta)$. Past research has shown that this can be experimentally determined and used to locate impacts on fiber reinforced composite plates by including the known relationship between the unknown source location and the sensor locations [115, 116]. The partial model approaches provide the benefit only having to know a portion of the dispersion properties of the medium. Most of the previously referenced footstep localization research falls in this category since an appropriate wave speed is selected prior to localization. It is important to note, however, that many of the cited studies on plate localization intentionally use the less dispersive higher frequencies for localization to minimize distortion.

Approaches that do not use any kind of model have also been implemented for plate localization. This is accomplished by using additional sensors so that Eq. (2.4) or Eq. (2.19) can be resolved without any knowledge of the group velocity. This has been done using the CWT to

separate individual frequency components [117], or as part of the group velocity function over the entire bandwidth [118, 119]. This method works in isotropic, homogeneous media because the additional sensors are independent of $c_g(\omega)$ and allow it to be incorporated into the localization problem as another unknown variable. The previously mentioned footstep localization done in [61] falls into this category, with c_g assumed as a constant and iteratively solved for. An alternative method was presented in [120] which does not use the typical formulation of the localization problem. As the previous methods, this assumes an isotropic and homogenous media, but uses the arrival time-difference among frequency components to estimate a dispersion curve for a hypothetical location as opposed to solving for the location manually. This processes is repeated iteratively until a location that produces the dispersion curve with the least variance is found, which is then taken to the be source.

These methods work well in environments where the wave speed is unknown, but the media is homogenous and isotropic, since there is one group velocity function which governs all of the time-difference equations (i.e., Eq. (10) is valid). If the structure is not isotropic or homogenous (e.g., a building environment), then the group velocity seen by the sensor depends on the frequency, angle, and distance, and $c_g = c_g(\omega, \theta, r)$. The problem then becomes mathematically unresolvable due to each sensor having its own unique group velocity function. For example, in this environment Eq. (2.3) becomes

$$c_{g,i}(t_i - t_0) = \sqrt{(x_i - x_0)^2 + (y_i - y_0)^2} \tag{2.20}$$

where $c_{g,i}$ is the group velocity from the source to the i^{th} sensor. Here there are always $N + 3$ unknowns for N equations, and cannot be resolved regardless of the number of sensors used. One

study, however, implemented a technique to overcome this issue [121]. The approach has the very reasonable assumption that two sensors which are close together should have very similar group velocities. Implementing this technique requires a minimum of $N = 6$ sensors and results in 6 unknowns: 3 equal pairs for the group velocities, x_0, y_0 and t_0. This method can be appreciated for having the fewest assumptions for a building environment, requiring only that sensors be paired relatively close to one another to assume a constant group velocity.

2.8. Conclusion

This chapter formulates the problem of using vibrations for indoor footstep localization using prior literature. The localization problem is first outlined with an emphasis on TDOA to supply a background to the problem. As with previous literature, the building floor is simplified as a plate. The dispersion properties for generalized concrete are considered. Prior research on footstep loading is applied and found to reduce the complexity of the problem to one of thin plates. The calculation of time-differences for localization are considered in this complex environment and are shown to yield inconsistent results. The effects of both structural and nonstructural elements in the building are examined for their effects on wave propagations. The resulting dynamics are considered to be similar to those of an isotropic, inhomogeneous plate. Lastly, localization in this type of environment is compared to prior literature on plate localization, where multiple techniques are discussed for their applicability to locate indoor footsteps.

In the next chapter, localization in a plate is implemented using the traditional TDOA approach via simulations. The accuracy of the results along with the effects of reflections from the boundaries are considered as contributing factors to the difficulties surrounding the localization problem.

Chapter 3 Thin Plate Simulation

3.1. Introduction

In the previous chapter, the numerous factors that add additional complexity to indoor wave propagations were discussed, such as boundary reflections, the inhomogeneous nature of concrete, and the effects of various other building elements that occur along the paths from the source to the sensors. Multiple plate localization techniques were discussed for their applicability to the indoor localization problem. In this chapter, simulations for localization are considered using traditional TDOA techniques using peak-detection and cross-correlation. Previous work in plate localization does not discuss at length the erroneous results obtained when using TDOA techniques. The purpose of this chapter is to elucidate the localization errors for TDOA techniques in a dispersive environment where significant wave reflections are considered. The accuracy limitations of localization based on time difference of arrival (TDOA) and hyperbolic localization is investigated in a noiseless simulation environment for an isotropic homogenous plate where significantly large boundary reflections are considered in a dispersive media. The following sections discuss the finite element model (FEM) and method used for simulations, followed by the techniques used for localization and simulation. Finally, results are presented and discussed.

3.2. Modeling and Simulation

A FEM is used to simulate plate dynamics due to an applied transient load. The square plate dimensions are 124 cm with a thickness of 6.35 mm. The material properties used are

intended to represent that of medium-density-fiberboard (MDF) with Young's modulus $E = 4\ GPa$, density $\rho = 736\ kg/m^3$, Poisson's ratio $\nu = 0.25$. The properties and dimensions are chosen to reflect those of an actual MDF plate, which will be used for a future experiment. The FEM contains 10,000 linear CQUAD4 elements that contain 4-nodes with three translational and two rotational degrees of freedom each. This results in 10201 nodes and a total 51,005 degrees of freedom. To model this transient excitation MSC Nastran solution 109, Direct Transient Response, is used with a time step of $1x10^{-4}$ for 0.6 seconds resulting in 6001 time steps. The simulation response is shown for several time intervals in Figure 3.1. To provide an impulse response, an out of plane force with duration of one time step and amplitude of 1 pound-force is used to excite all frequencies of the system up to 500 Hz, and band-limited to ensure a minimum of 4 elements/wavelength. Direct transient response analysis does not permit the use of complex coefficients. Therefore, structural damping cannot be used and has to be evaluated by means of equivalent viscous damping. A relation between structural damping and equivalent viscous damping was defined using the first mode of the system and 1% structural damping. The configuration of sensors and impact locations is shown in Figure 3.2 for two sensor configurations. For the first configuration, sensors are placed more inwards toward the board, while the second configuration has all sensors closer to the boundaries. The simulation measures acceleration.

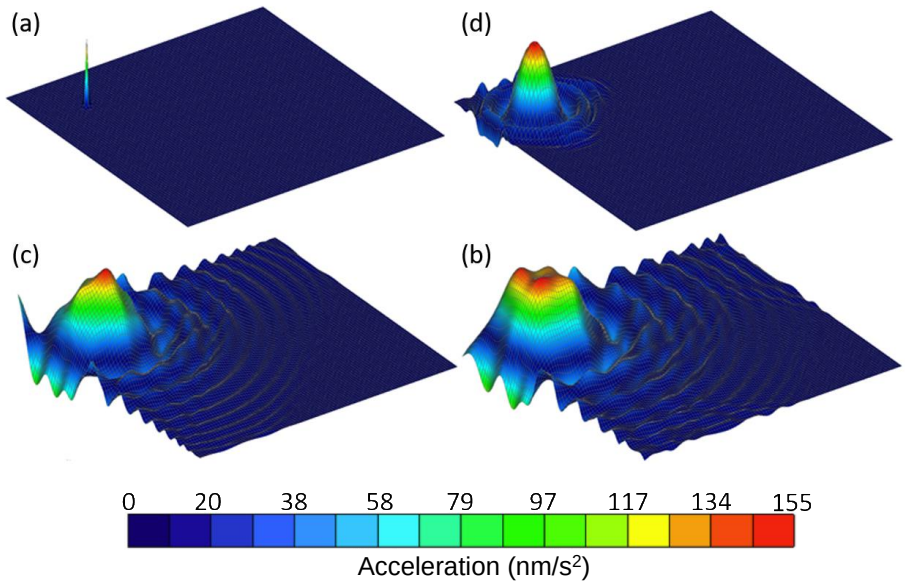

Figure 3.1. Simulation response of a plate under an impact load: (a) Impact simulation at *t = 0* (b) response at *t =7.2 ms* (c) response at *t = 24.1 ms* and (d) response at *t = 30.6 ms*.

The accuracy of the localization algorithm is assessed by the overall root-mean-square error (RMSE), which is calculated:

$$RMSE = \sqrt{RMSE(X)^2 + RMSE(Y)^2}\,, \tag{3.1}$$

where $RMSE(X)$ and $RMSE(Y)$ are the root-mean-square error of the x and y coordinates respectively. To assess the consistency of the perceived wave speed based on the known true distance-difference values, the coefficient of variance (COV) among all perceived velocities is used. It is not necessarily the case that the COV corresponds directly to accuracy, but provides insight into the consistency of the perceived wave speed, which is highly correlated to the accuracy of the calculated time-differences. The perceived wave speed is calculated as the known distance-difference over the measured time-difference. The COV is determined by σ/μ, where σ and μ are

the standard deviation and mean of the perceived wave velocity, respectively. In addition to the RMSE and COV, the signs of arrival (SOAs) are considered. The SOA between any two sensors is either 1, -1 or 0, dictated by which sensor received the signal first, or at the same time for the case of 0. This can be used to create a spatial grid of separation lines between each sensor pair and reduce the solution to some area defined by the grid [52].

Attempts to locate impacts are made by estimating the TDOA between sensors using either cross-correlation or a peak-difference method (subtracting the peak response time between two sensors). Hyperbolic localization is used over a span of wave speeds with the algorithm described in [68], using the lower left sensor in both configurations as the reference. This localization process is repeated for both sensor configurations, with those closer to the boundaries expected to experience more variation due to higher reflection intensities.

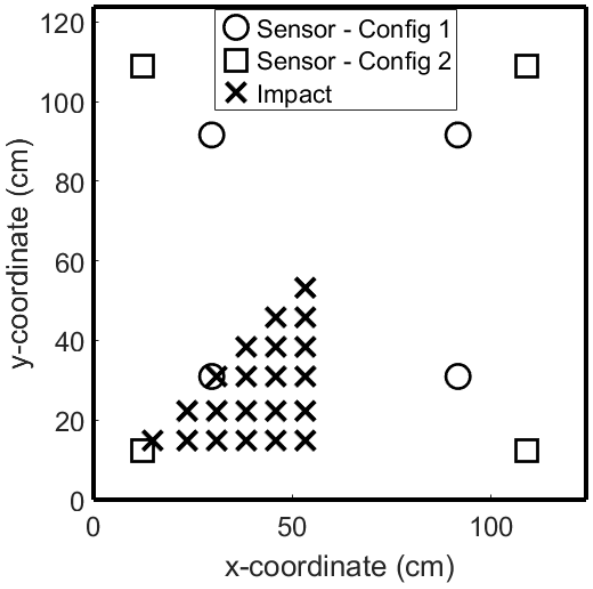

Figure 3.2. Impact and sensor locations for two different sensor configurations. All 21 impact locations are simulated for each sensor configuration case.

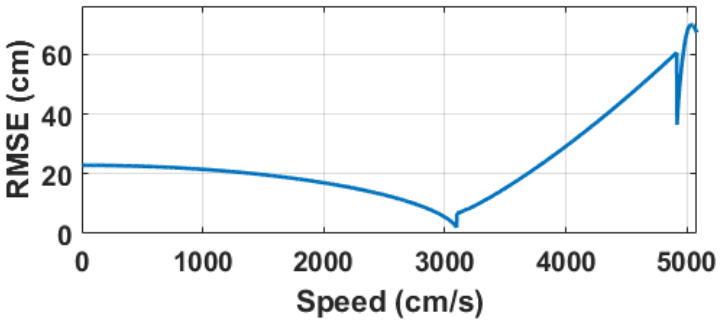

Figure 3.3. RMSE over velocity range for the example case of an impact originating at (45.7, 31.0) and TDOA errors of ± 1 ms.

Next, an example is presented and discussed for a constructed case with small TDOA errors. The RMSE from hyperbolic localization is examined, along with the COV and SOAs from the time-difference. Consider a case of the impact originating from (45.7, 31.0) with the first sensor configuration. The true distance-differences are calculated using the bottom-left sensor as the reference, and are 29.7, 46.7 and 59.9 cm. between the lower-right, upper-left, and upper-right sensors respectively. That is to say, the bottom-left sensor is 29.7 cm. closer to the impact location than the bottom-right sensor, 46.7 cm. closer than the top-left sensor, and 59.9 cm. closer than the top-right sensor. Assuming a wave speed of 3810 cm/s, the corresponding time differences would be 7.80, 12.3 and 15.7 ms. Applying a small TDOA error of $\pm$ 1 ms, new TDOAs are calculated as 8.9, 11.3 and 16.7 ms. The perceived propagation velocities determined by dividing the true distance-differences over the new time-differences are then found to be 3378, 4148 and 3581, yielding a COV of 0.108. Without any errors in the TDOAs, all velocities are 3810 cm/s (the assumed value), and so the COV is 0. The SOAs are retained as all positive since the magnitude of the TDOA errors ($\pm$ 1 ms) is not greater than any of the TDOAs (and therefore will not affect the sign). Due to the errors introduced to the TDOAs, the assumed wave speed of 3810 cm/s may

not provide the most accurate result. This is shown in Figure 3.3, where the RMSE is calculated over a range of 2540 to 5080 cm/s. The speed range used here is arbitrarily selected based on the perceived propagation velocities. The minimum RMSE of 2.03 cm is found at a velocity of 3096 cm/s. The hyperbolic results for this small TDOA error case is shown in Figure 3.4, with the true impact location highlighted in blue. Each hyperbola corresponds to a sensor pair, where the solution is at the intersection.

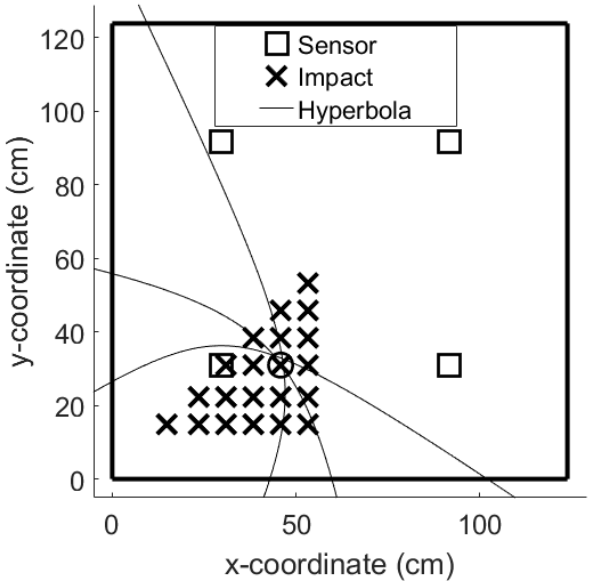

Figure 3.4. Hyperbolae resulting from TDOAs with ± 1 ms error and a wave speed of 3048 cm/s for an impact at (45.7, 31.0) (circled).

3.3. Results and Discussion

A sample response of the first 40 *ms* as seen from location (29.7, 31.0) and (91.4, 91.4), is shown in Figure 3.5 for an impact at the location in (38.1, 38.1). The first "sensor" is significantly closer to the impact, and the initial waveform and its reflection can be seen. The second sensor is

much further, where the waveform has significantly dispersed and the reflection is not observably separate. The time-difference of arrival calculations for both methods and sensor configurations are found to be significantly erroneous, resulting in poor localization results. In order to calculate an RMSE for time-difference methods, an assumed propagation velocity must first scale the time delays. In non-dispersive media (e.g. air), there is only a single propagation velocity for all frequency content of the input signal. This is not the case for dispersive media, where the dispersion relation governs the phase velocity, and so a single velocity must be selected with the desired trait of having a minimum RMSE. Because of this, the application of TDOA method to dispersive media requires the wave speed assumption be tuned to a specific velocity. This presents an issue for large TDOA errors, since the results are inaccurate for all wave speeds, and thus at very low speed scales, a small distance-difference is observed, and the solution approaches the point with the smallest distance-difference that minimizes the error function of the hyperbolic estimator. Depending on the geometry of the sensors, it is possible for this low wave speed solution to result in the minimum RMSE, regardless of the impact location. For the plate used in this simulation, the center of the plate is resolved as the best solution for very low wave speeds, and so produces the smallest RMSE. Conceptually, this issue is more likely to arise when the source is near the sensors, as the solution to the smallest difference-distance is not likely the minimum RMSE when the source is far from the sensors. The average accuracy for all impact locations is assessed over the entire velocity range 3 to 7620 cm/s, which corresponds to the phase velocities derived in [122] for a thin plate of these properties. This is done to verify that no particular velocity assumption results in low RMSE results for all impacts. The dispersion curve of the flexural wave mode in the 500 Hz bandwidth of interest is shown in Figure 3.6 along with the averaged power spectrum over all impacts for all sensors.

The RMSE results are shown in Figure 3.7; however, they are not a good measure of the accuracy of the TDOAs due to indiscriminate outliers. For example: the RMSEs for cross-correlation in the second configuration are orders of magnitude above the first configuration because of one particular impact case. Since the reliance of any localization method is of considerable importance, all outliers are retained, particularly since this is a noiseless environment, and thus the outliers are not stochastic. Since the localization results are abject, instead the coefficient of variation (COV) is considered for the perceived propagation velocity, along with the number of SOA errors. The COV represents the consistency of the perceived propagation velocity, i.e.: the ability to scale the time-differences by a single wave speed and get accurate results, while the number of SOA errors represents the ability to accurately discern a wave source as originating from one side or another for any sensor pair.

Considering the RMSE over the entire velocity range, there are several drops in the error as the velocity increases. These drops are either associated with wave speeds that dominate that response, or more involved events that occur due to the nonlinear nature of hyperbolic localization. An example of this is shown in Figure 3.8 for a particularly good localization case (COV 0.081), where we see RMSE values below 2 inches for a wave speed of 2050 cm/s. The low COV accurately suggests the existence of a particular wave speed that provides accurate results. The drops in RMSE above the ideal wave speed are inconsistent, and can be recognized by the gradient leading up to a particular drop off. Several other cases are included for comparison, showing inconsistency in which wave speed produces the minimum RMSE. Examining the two impacts at (23.5, 14.9) and (31.0, 22.3), the error of the calculated TDOAs are so large that no wave speed solution is better than assuming the middle of the plate as the source.

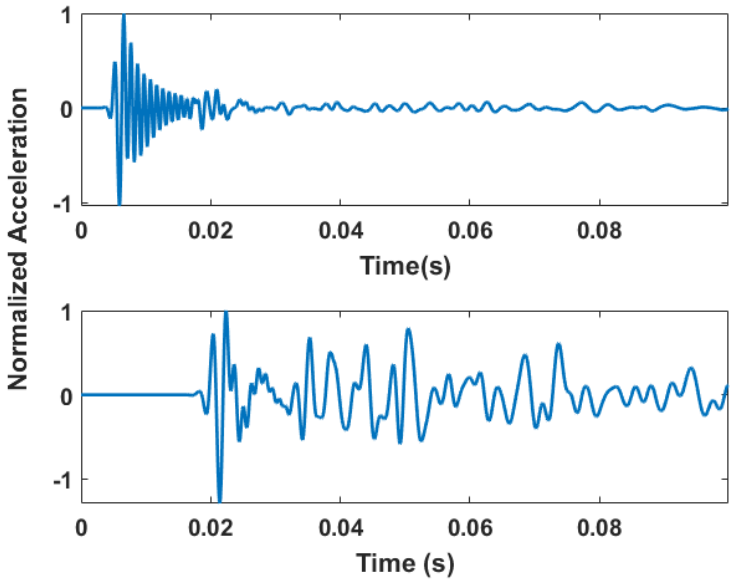

Figure 3.5. Time trace of acceleration response as seen at the point located at (29.7, 31.0) above and as seen at the point located at (91.4, 91.4) below for impact at location (38.1, 38.1).

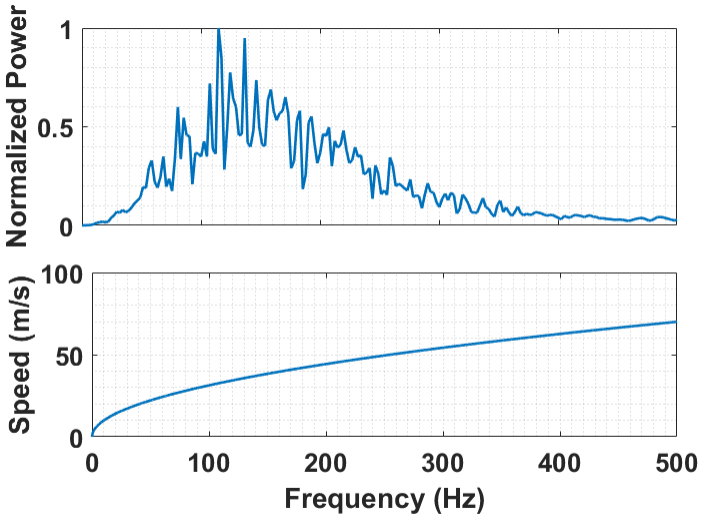

Figure 3.6. Averaged power spectrum over all impacts and sensors; dispersion curve for the flexural wave mode.

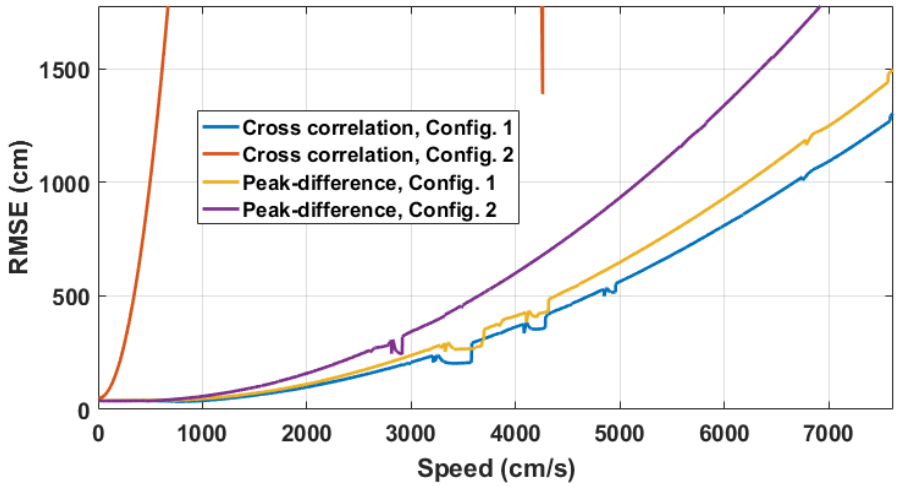

Figure 3.7. RMSE over a 7620 cm/s velocity range for two TDOA methods and two sensor configurations.

The percent error for SOAs represents the percent of SOAs that are reported incorrectly out of 126 (6 sensor pairs, 21 impacts), and is a good measure of the ability to isolate the source to an area by constructing a grid of sensor pairs. For the cross-correlation method in the first configuration, there is a COV of 0.79, with 7.1 % error of SOAs. In the second configuration, the COV increases to 2.81 (highly variable wave speed), and the SOAs error also increases to 8.7 %. This suggests that the increase in reflections from the boundaries in the second configuration increases the variance in the perceived wave speed and reduces the ability to isolate the source to an area from the SOAs.

For the peak-difference method in the first configuration, there is a COV of 0.74, and SOAs error of 4.0 %, while the second configuration has a COV of 4.68 with 9.5 % SOAs error. This shows a similar trend as the cross-correlation method between the first and second configurations: that the increase in reflections increases the COV and SOAs error. A noticeable difference in the peak-difference method, however, is the magnitude that the COV and SOAs

increase between the first and second configurations, suggesting that the accuracy of the peak-difference method may be more negatively affected when reflections are significantly large.

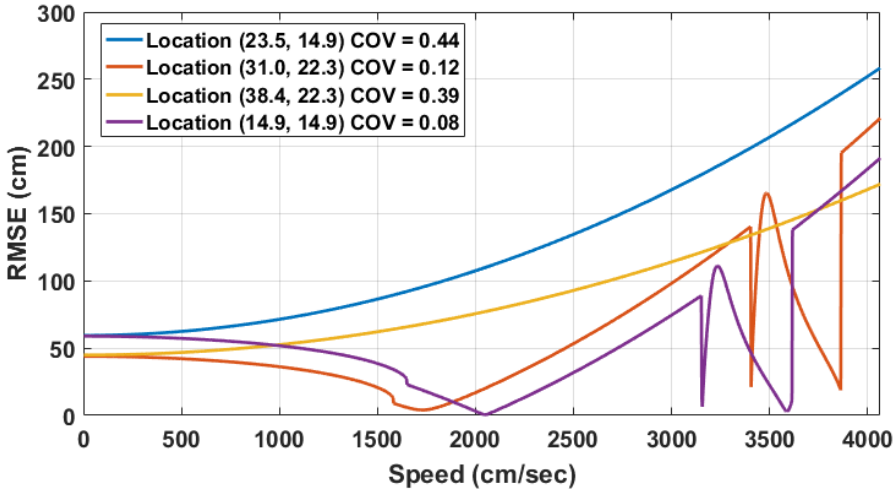

Figure 3.8. RMSE over a portion of the velocity range for several select impacts. The most accurate velocity changes based on impact location: 2050 cm/s and 1730 cm/s for impacts at (31.0, 22.3) and (38.4, 22.3) respectively.

For both cases, moving the sensors closer to the boundaries decreases the overall accuracy. When the sensors are very near to the boundaries and reflections are large, it appears that the cross-correlation method may perform better than peak-difference. This could be the result of the symmetry of the structure since all sensors are symmetric at the boundaries, the convolution of the reflections could yield an approximation of the time-difference. The SOAs are relatively accurate in all cases, with only a small percentage of signs being interpreted incorrectly, suggesting that when heavy reflections are present in the signal, the SO-TDOA algorithm would still perform well, and could be used to locate the source to a specific area.

3.4. Conclusion

Wave reflections play an important role in the accuracy of localization algorithms in dispersive media. When reflections are significantly large, neither cross-correlation nor peak-difference methods produce accurate localization results. The peak-difference method was found to perform better when the sensors are further from the boundaries, while cross-correlation results appear slightly better when the sensors are near the edge. This suggests that cross-correlation may be a preferred tool if reflections are sufficiently large. The SOAs have less than 10% error for all cases, suggesting good accuracy despite large TDOA errors. In the next section, the two TDOA techniques are compared using dispersion compensation in a building environment. Several parameters are studied and varied to find optimal performance. Due to the accuracy results being significantly better, COV and TDOA are excluded and evaluations are based instead on the average localization error.

Chapter 4 Implementation in Goodwin Hall

4.1. Introduction

In this chapter, a dispersion compensation tool is implemented in a building experiment and compared traditional TDOA methods. Observations of dispersion in Goodwin Hall are considered and used to estimate the dispersion relation. The results are evaluated for accuracy using a well-known hyperbolic localization algorithm and compared against traditional localization techniques based on TDOA acquired using peak-detection and cross-correlation. The effect of dispersion compensation on localization accuracy in this environment is evaluated and discussed. The purpose of this chapter is to investigate the preliminary effects of dispersion compensation for localization in a real-world building environment. By doing so, insight is provided into the capabilities of structural instrumentation systems for localization when dispersive wave theory is considered.

4.2. Experiment

The conducted experiments leverage Virginia Tech's Goodwin Hall, a newly constructed five-story, 160,000 ft^2 public smart building. Goodwin Hall is instrumented with over 200 structurally mounted accelerometers connected to five VTI Instruments data acquisition systems distributed throughout the building. The acquisition systems are fully synchronized with two Oregano Systems transparent switches. This smart infrastructure acts as a real-world living laboratory, providing research opportunities for both faculty and students.

Testing took place on the 4th floor of Goodwin Hall in a more densely instrumented corridor, shown at the top of Figure 4.1. Fifteen PCB shear accelerometers (single-axis, model no. 393B04) were used to measure the vibrations induced by an impact hammer strike (Kistler modal hammer model no. 9727A500). All of the accelerometers are structurally bonded to the supporting I-beams underneath the fourth floor.

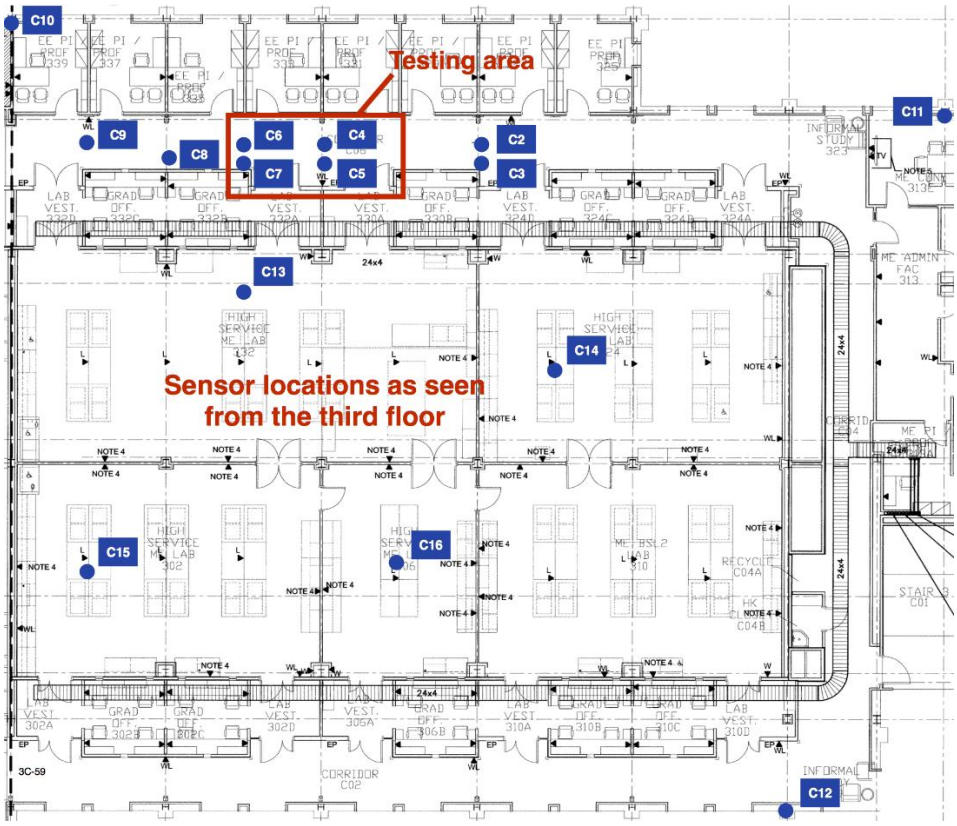

Figure 4.1. Sensor locations as seen from the third floor. Sensors labeled C-2 to C-16, corresponding to the channel number. Testing took place in the area covered between sensors C-4 and C-7.

Figure 4.2 shows an example of one of the welded mounts with 3 single-axis accelerometers. For this experiment, only the vertical axis (normal to the floor) is used. The accelerometers are labeled according to their corresponding channel: C-2 through C-16, with C-1 occupied by the impact

hammer. Five impact locations were selected relative to sensor position, labeled A-E in Figure 4.3. For these experiments, the sensor labeled C-10 has been arbitrarily selected as the origin. The two-dimensional coordinates of the sensors used in this study are shown in Table 4.1. Data was collected synchronously at a sampling frequency of 4267 Hz. Using a nylon tip on the impact hammer, points A-E were struck 10 times each. The same process was repeated for points A, B and E, using the steel tip, totaling 8 different impact scenarios. The acquisition system was set to pre-trigger 100 samples (0.023 s) prior to the impact.

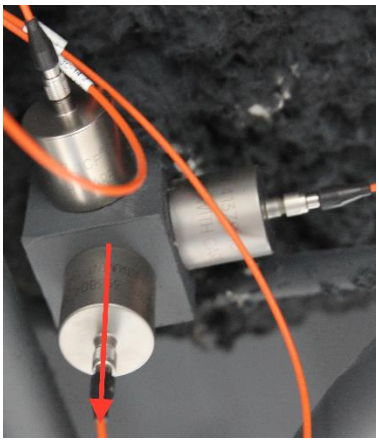

Figure 4.2. Example of a sensor mount in Goodwin Hall with 3 single-axis accelerometers (model PCB 393B04). Only the vertical axis (red) is used in this study.

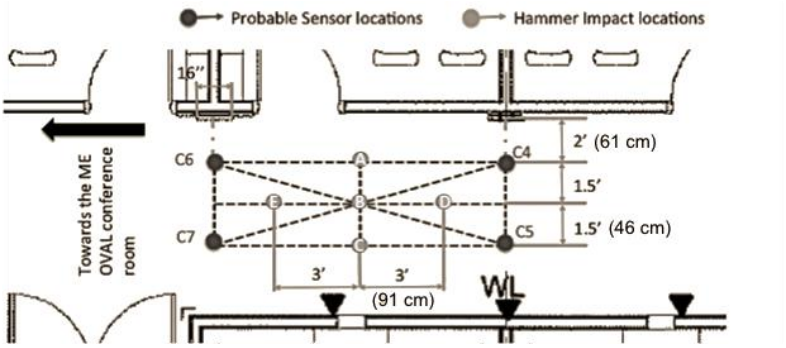

Figure 4.3. A layout of the immediate testing vicinity is shown, which is a small portion of the full monitored area. Impact locations are labeled A-E. Four of the 15 sensors used are visible, labeled C4 - C6.

Table 4.1. Sensor and impact locations using C-10 as reference.

	Coordinates (m)			Coordinates (m)	
Label	X	Y	Label	X	Y
C-2	30.1	31.3	C-12	42.8	4.1
C-3	30.1	30.7	C-13	20.5	26.2
C-4	23.7	31.4	C-14	33.8	23.9
C-5	23.7	30.6	C-15	13.8	15.8
C-6	20.5	31.4	C-16	26.8	12.9
C-7	20.5	30.6	Point A	22.1	31.5
C-8	17.3	30.6	Point B	22.1	31.0
C-9	14.1	31.4	Point C	22.1	30.5
C-10	10.7	36.1	Point D	23.0	31.0
C-11	49.0	34.2	Point E	21.2	31.0

4.3. Dispersion Compensation for Localization

To reduce the adverse effects of dispersion in the measured signals, time-to-distance domain mapping (TDDM) [109] is used. This removes the effects of dispersion that make time-difference calculation difficult, effectively enhancing the accuracy of the distance-difference relationship obtained from cross-correlation. To implement this numerically, the known frequency-wavenumber relationship is used to map the measured signal to a new set of equally spaced points in the wavenumber domain. An example of this is shown Figure 4.4, which compares a wave measured at two different distances before and after frequency warping. The data used for this example was created analytically using the known properties of aluminum. In practice, the TDDM is implemented by first taking the Fourier transform of the signal. Then, using the known dispersion relation of the media, the Fourier transform is resampled at points equidistant in the wavenumber domain (as opposed to the frequency domain). Then the inverse Fourier transform is

applied to the resampled signal to obtain the new signal in the distance domain. A step-by-step guide for implementing this is provided in the reference for TDDM.

After implementing TDDM, the new warped signals look nearly identical to each other, with a difference only in the location along the abscissa. The resultant signals appear smeared in the distance domain, which is a result of the measured time-trace not starting at the exact time of excitation which causes a linear phase shift. This is representative of what would be seen in a real localization scenario, where the start time of the excitation is unknown. From the context of localization, calculating the distance-difference seen here can be easily determined with cross-correlation, yielding exactly a 3 m separation. This technique has been successfully applied to locate impacts in plate-like structures in prior literature [73, 114]. Although effective, the TDDM algorithm does not remove the presence of reflections, which still produces a source of difficulty in implementing localization.

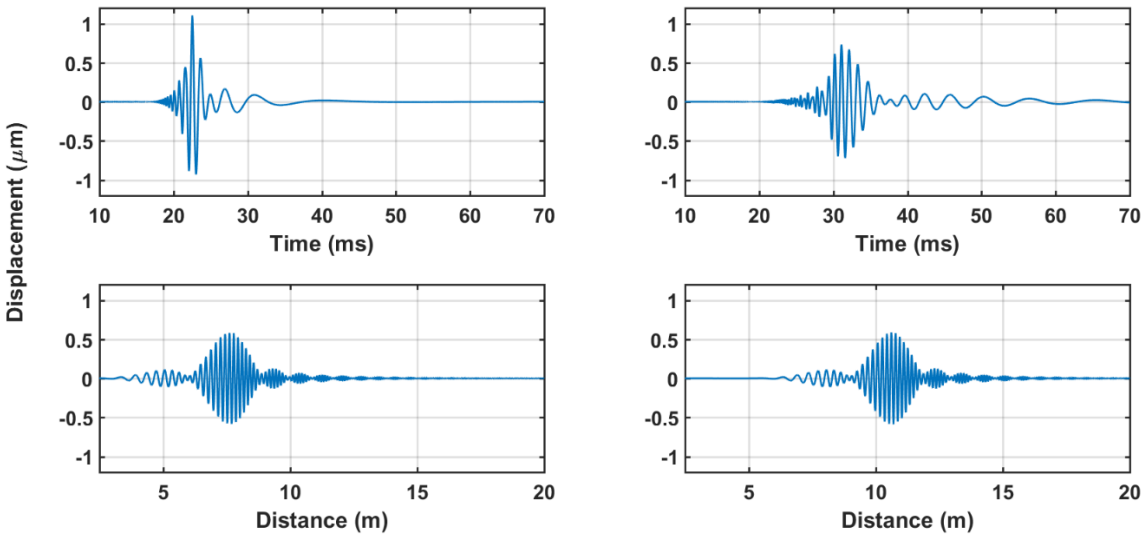

Figure 4.4. Time trace (top) and dispersion compensated distance-trace (bottom) for measurements taken 2 m (left) and 5 m (right) from the source.

4.4. Dispersion observation

The dispersion characteristics of the medium are estimated prior to localization in order to implement dispersion compensation. A preliminary assessment of the dispersion in Goodwin Hall is estimated using the spectrogram. Spectrograms of several sensors at increasing distances from the source area are shown in Figure 4.5. Sensor C-4 (4.5a) is the nearest to the source, and shows most of the spectral content arriving very close together in time. As distance progresses, the dispersion relation becomes more obvious while the signal quality simultaneously degrades (4.5c). Intuitively, after a certain distance the signal quality has degraded to a point where the dispersion relation is barely visible (4.5d). It is assumed that the degradation effects are due to a combination of damping, anisotropic reflections, and nonlinearities (cracks, joints, etc.) that occur along the path from the source to the sensor.

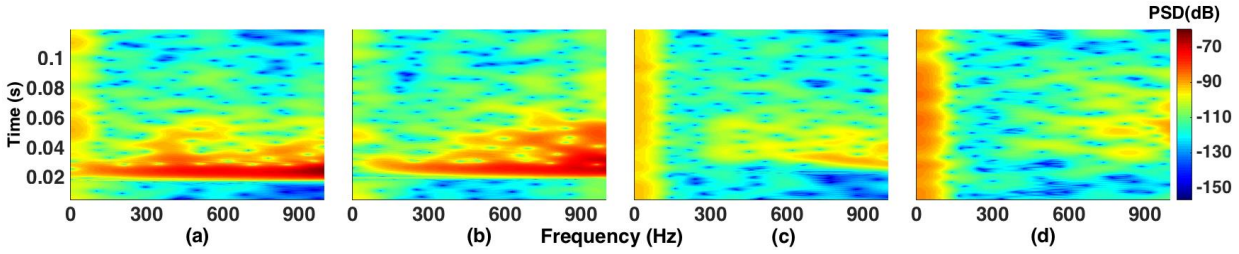

Figure 4.5. Spectrograms of the measured vibration response for several sensors at increasing distance. From left to right: 2.5 m, 3.90 m, 11.7 m, 18.8 m. A hammer impact at location B is the excitation source. The spectrograms are formed using a 12 ms Hamming window and 98% overlap.

The dispersion curve is estimated using the results from the STFT series. For a single sensor, each frequency component has a point in time where its energy is at a maximum. Using the impact at location B as a known reference, the distance-difference between sensors can be calculated. By comparing two sensors, the difference in time of maximum energy for an individual

frequency component can be divided over the known distance-difference. This provides a distribution of the group velocity at each frequency. Experimental verification of the concrete properties in Goodwin Hall would be site-specific and difficult to implement due to the nature of concrete, thus parameters are selected that best-fit the experimental velocity distribution ($E = 44.7\ GPa,\ b = 75\ mm,\ \rho = 2722\ kg/m^3$). To estimate the dispersion relation, Eq. (4) is fit via least squares to the mean velocity measured at each frequency up to 1.0 kHz. The result shown in Figure 4.6 fits the data well in the low frequency range below 400 Hz, and with reasonable estimates of the concrete properties in Goodwin Hall. The property estimates of the concrete in Goodwin Hall are: $E = 39.4\ GPa,\ b = 90\ mm,\ \rho = 2443\ kg/m^3$. There are significant limitations when using a spectrogram to perform this time-difference analysis. The 12 ms window length leads to poor time resolution for short-lived high frequency content, and is limited in capturing low-frequency content. Additionally, the complexity of the building structure limits the applicability of the thin plate assumption for higher frequencies. The nature of the spectrogram process is also biased toward assuming lower velocities at higher frequencies. This occurs when the time-difference is less than 1 window length, or 12 ms, which discretizes the time-difference to 0, and must be removed for averaging. The dispersive relationship obtained here is used as an estimate to implement TDDM for localization. Since the curve is calculated to fit estimated wave speeds below 1.0 kHz, content up to the Nyquist frequency (2.1 kHz) is extrapolated.

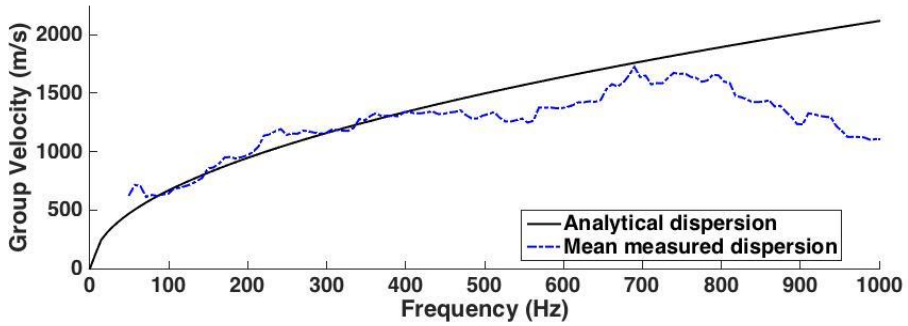

Figure 4.6. Experimental estimate for the dispersion relation in Goodwin Hall using response measurements from impacts at Point B. The analytical curve is found using thin-plate theory with a least-squares fit.

4.5. Results

Localization is performed using three different distance-difference methods: peak-difference, cross-correlation, and warped-correlation. Accuracy is considered against several localization parameters, which are selected based on which time-difference method is used. Since the peak-difference and cross-correlation methods both require an assumed wave speed, a range of speeds will be used to determine which speed offers the best-case scenario for localization. The range of speeds used is from 10 m/s to 2750 m/s. This range was selected based on the range of velocities expected using Eq. (4), and extended beyond that range for good measure. This is similarly done for the warped-correlation method, but since this method utilizes the frequency dependence of wave speed, the entire dispersion curve is scaled by a "scale factor." The scale factor ranges from 0 to 4.0, which was selected to help insure the global minimum is found. This is discussed in more detail in Section 5.4. Additionally, since the effects of reflections on the signal may cause only a portion of the signal to be useful, different portions of the signal are used as well. The data portion is considered for all three methods, and uses a step size of 2.3 ms. The average error is calculated over 10 trials, for each scenario as

$$\mu_{error} = \frac{1}{10}\sum_{i=1}^{10}\sqrt{(x_0 - x_i)^2 + (y_0 - y_i)^2} \quad , \tag{4.1}$$

where x_i, y_i and x_0, y_0 are the coordinates of the sensor and impact location, respectively.

Several different methods of analysis are used to determine the accuracy of each method. First, an approach similar to leave-one-out-cross-validation is considered [123-125], where each of the eight impact scenarios is localized based on the tuning results of the other seven. Each method is then considered in a more active tuning process to gain insight into the potential accuracies of each method with several levels of tuning. Three different tuning cases are considered: (1) parameters selected to minimize the average error across all impact scenarios (N=80); (2) parameters selected to minimize the error for each location (N=10); and (3) parameters selected to minimize the error for each impact (N=1). Each basis for error minimization is referred to as "global", "per-scenario", or "per-impact," respectively. Prior to localization, a 6th order bandpass Butterworth filter is applied with a lower cutoff frequency of 640 Hz, and an upper cutoff frequency of 850 Hz. This bandwidth was selected as it was found to have the highest signal-to-noise ratio (SNR) and provided the best performance increase among all three methods. Unfortunately, the measured dispersion does not adhere well with the analytical solution in this bandwidth. The effects of this are partially alleviated by using the variable scale factor on the dispersion curve used for compensation.

4.5.1. Leave-One-Out Cross Validation

To validate the accuracy of each method in locating the hammer strikes, each of the eight impact scenarios is localized based on the tuning results of the other seven. This provides a more realistic estimate of the accuracies in each method. The results are shown in Table 4.2. The warped-correlation method is found to perform better than either of the other methods, while using cross-correlation alone provides the worst performance.

Table 4.2. Error averaged over 10 impacts for each scenario using cross-validation.

Time-difference Method	Error per impact scenario in cm								
	A		B		C	D	E		Average
	Steel	Nylon	Steel	Nylon	Nylon	Nylon	Steel	Nylon	
Peak-difference	126	112	471	108	165	175	81	253	186
Cross-correlation	415	27	90	409	23	359	340	101	221
Warped-correlation	219	35	168	203	20	380	189	112	166

4.5.2. Peak-Difference Method

With the peak-difference method, arrival-time differences among the accelerometers are calculated by subtracting the time of peak response between them, using sensor C-2 as the arbitrary reference. The localization algorithm is evaluated for various assumed wave speeds and data portions, and is found to be most accurate at 1470 m/s and 170 samples (40 ms), with an average error of 1.86 m. Selecting the parameters which minimize the error for each location reduces the error to 1.52 m; repeating the process for each impact, the average error reduces to 0.81 m. The results are presented in Table 4.3. The average error as a function of these parameters is shown in Figure 4.7.

Table 4.3. Error averaged over 10 impacts for each scenario using peak- detection.

Basis for error minimization	Error per impact scenario in cm								
	A		B		C	D	E		
	Steel	Nylon	Steel	Nylon	Nylon	Nylon	Steel	Nylon	Average
Global (N=80)	126	112	471	108	165	175	81	253	186
Per-scenario (N=10)	102	99	357	93	109	166	78	210	152
Per-impact (N=1)	35	45	255	31	45	69	19	153	81

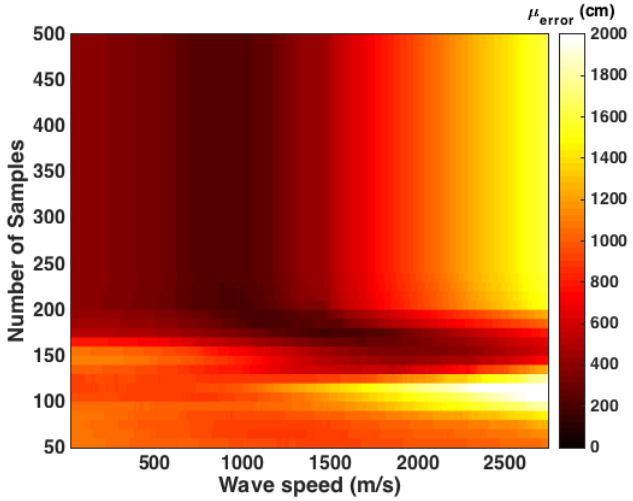

Figure 4.7. Localization error averaged over 80 impacts for various speeds and portions of data using the peak-difference method. The global minimum is found at a speed of 1470 m/s retaining the first 170 samples of the signal.

4.5.3. Cross-Correlation Method

For the cross-correlation method, the arrival-time differences among the accelerometers are calculated by convolving the two waveforms (with one being time-reversed) and finding the lag-time at peak correlation. Since the received time-trace contains the propagating waveform along with reflections, only a portion of the measured signal is used. The accuracy is evaluated for different portions of data as well as wave speeds. The total averaged error is shown in Figure 4.8. A minimum error of 2.21 m is found using a speed of 1130 m/s and 200 samples (47 ms). If the

proper wave speed and cut-off time (number of samples) could be selected for each impact, then this error reduces to 0.54 m. The results are shown in Table 4.4.

Table 4.4. Error averaged over 10 impacts for each scenario using cross-correlation.

Basis for error minimization	Error per impact scenario in cm								
	A		B		C	D	E		
	Steel	Nylon	Steel	Nylon	Nylon	Nylon	Steel	Nylon	Average
Global (N=80)	415	27	90	409	23	359	340	101	221
Per-scenario (N=10)	171	19	65	164	14	80	15	65	74
Per-impact (N=1)	133	6	53	136	4	39	14	44	54

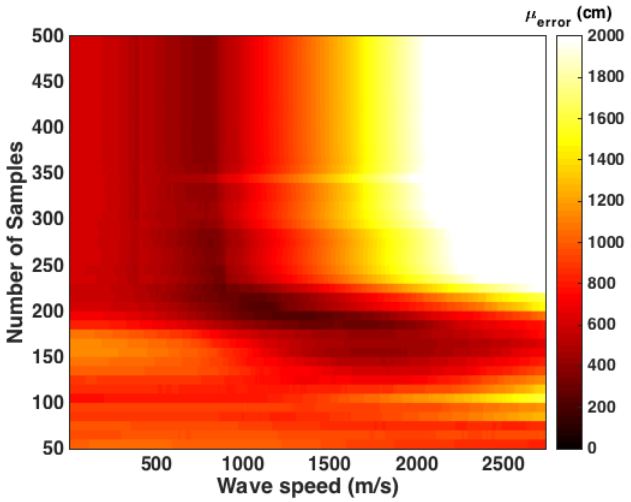

Figure 4.8. Localization error averaged over 80 impacts for various speeds and portions of data using the cross-correlation method. The global minimum is found at a speed of 1130 m/s retaining the first 200 samples of the signal.

4.5.4. Warped-Correlation Method

For the warped-correlation method, dispersion compensation is applied to the measured signals prior to convolution. Figure 4.9 shows a sample of time-data that has been remapped to the distance domain. The remapped signal is still distorted due to the unknown time delay, but the dependence on distance has been removed. The velocity function is multiplied by a variable scalar,

similar to using a range of wave speeds for time-difference methods. This scale factor shifts the curve around its measured estimate. The scale factor ranges from 0 to 4.0, and was selected iteratively to fully encompass the prominent features and to ensure the global minimum is found. As with the cross-correlation method, the convolution is evaluated using a variable number of samples. The total average error results are shown in Figure 4.10. A minimum error of 1.47 m is found using 230 samples and a scale factor of 1.10. If the proper wave speed and number of samples could be selected for each impact, then this error reduces to 0.15 m. Since the notion of scaling the dispersion curve is unconventional, it is worth reporting that the when the scale factor is fixed to a value of 1, a minimum error of 166 cm is found at 230 samples. The results are shown in Table 4.5.

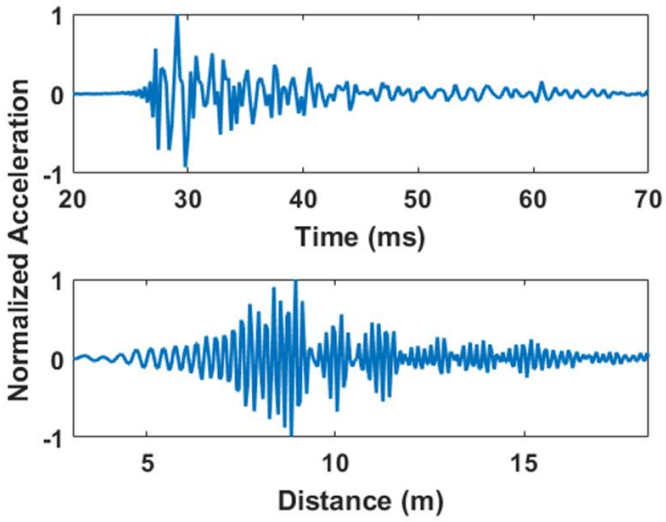

Figure 4.9. Example of the measured signal 8.84 m from impact location before (top) and after applying time-to-distance domain mapping (TDDM).

Table 4.5. Error averaged over 10 impacts for each scenario using warped-correlation.

	Error per impact scenario in cm

Basis for error minimization	A		B		C	D	E		Average
	Steel	Nylon	Steel	Nylon	Nylon	Nylon	Steel	Nylon	
Global (N=80)	196	33	161	180	18	360	128	101	147
Per-scenario (N=10)	116	21	69	47	12	110	14	69	57
Per-impact (N=1)	19	5	25	16	4	15	9	26	15

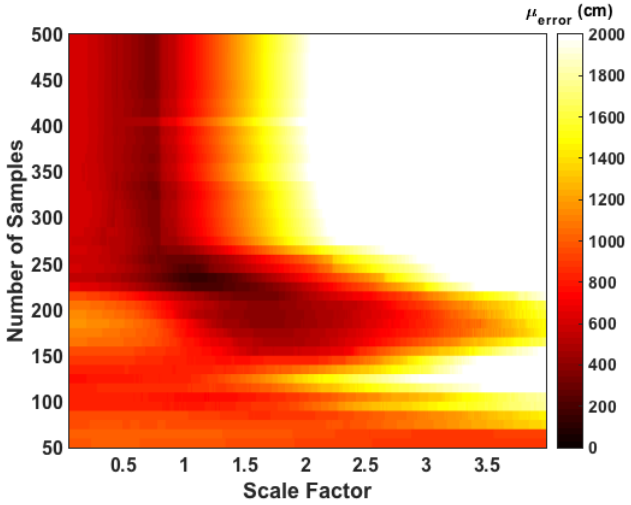

Figure 4.10. Localization error averaged over 80 impacts for various scale factors and data portions using the warped-correlation method. The global minimum is found with a scale of 1.10 and retaining the first 230 samples of the signal. Using a scale factor of 1, the averaged error is 166 cm.

4.6. Discussion

With the peak-difference method, the accuracy does not change after 230 samples (54 ms), which indicates the maximum value of the signal is no longer changing beyond this point. The fact that the optimal performance was found before this point (at 40 ms) suggests that the peak response of the data is not the best peak to select from, but that earlier time-difference methods. The cross-correlation method is similar, with few changes after the 230 samples. Since the optimal performance occurs before this point (at 47 ms), it is likely that the decrease in accuracy beyond

this point is due to reflections. While a similar effect is visible for the warped-correlation case, the samples cannot be compared due the conversion to the distance domain.

The average error for all three methods using cross-validation is found to be fairly similar: 1.86 m using peak-difference, 2.21 m using cross-correlation, and 1.66 m using warped correlation. The large errors relative to the closeness of several sensors is a product of both the low sampling rate used as well as the lack of any sensor selection algorithms. Incorporating the dispersion estimate via TDDM appears to improve the results, providing an increase in average accuracy of 20 cm compared to the peak-difference method, and 55 cm compared to the cross-correlation method. The improvement is not consistent for all locations and in some cases, provides worse results. The exact reason for this is unknown, however, it is likely due to the limitations of a uniform dispersion assumption, in addition to the various uncertainties present in all of the implemented methods.

Selecting the parameters that correspond to the minimum error shows the maximum potential accuracy of each scenario. The increase in accuracy for all cases is obvious when selecting best-case performance parameters, however, an interest lies in the relative performance of each case. Selecting the optimal parameters for each impact reduces the average error of each case to 81 cm, 54 cm, and 15 cm, for peak-difference, cross-correlation, and warped-correlation, respectively. This suggests that a better understanding of the non-uniform dispersion per sensor can lead to more accurate localization results. While the effects of noise are likely to contribute to the average error found during optimization, it is unlikely that noise is entirely responsible for these effects. Additionally, when optimizing only the portion of data used, and retaining a scale factor of one for the warped-correlation method, the average accuracy is 166 cm. This single-parameter optimization performs better than either the peak-difference or cross-correlation

methods, despite optimization over two parameters. The optimal wave speed for the peak-difference method (1470 m/s) is different than the optimal wave speed for the cross-correlation method (1130 m/s). The reason for this is not known precisely, however, it is likely due to differences in the way dispersion affects these methods.

Future work will investigate developing source-sensor dispersion characteristics within the building, along with developing relationships between measured characteristics (e.g., amplitude, spectral content) and optimization parameters. Using a higher sampling frequency has been done in a similar experiment for the peak-difference method [53], and would likely increase the performance for all three cases.

4.7. Conclusion

This chapter explores vibration event localization using under-floor accelerometers in a densely-instrumented building on the Virginia Tech campus, Goodwin Hall. Dispersion compensation is investigated as a useful tool to improve localization by traditional techniques such as TDOA. In a complex building environment, it is difficult to fully understand the underlying mechanism of wave propagations. The goal of this research is to provide insight into potential solutions while considering some of the more readily available techniques. Localization using peak detection, cross correlation, and dispersion compensated cross-correlation are compared in a cross-validation environment, and found to be accurate within 1.86, 2.21, and 1.66 m, respectively. Performing TDDM prior to cross-correlation appears to enhance the accuracy of localization in this environment, with performance being better than either peak-difference or cross-correlation. Differences are observed in the ideal wave speed when comparing cross-correlation and peak-

difference methods. The reasons for this are not exactly known, but are likely due to differences in the effects of dispersion. Optimally tuning localization parameters on a per-impact and per-scenario basis shows the best results for the warped-correlation method (0.15 m). This does give insight into the inhomogeneity of the floor, suggesting that wave propagation needs to be characterized in all directions. Based on the results, applying dispersion compensation prior to cross-correlation appears to be a promising avenue for indoor localization.

In the next chapter, a machine learning approach to localization is investigated using the k-nearest neighbors algorithm. A passive, localization system is implemented using accelerometers placed on the floor of a small area in Goodwin Hall. Several experiments are performed to classify the location of a variety of impacts as well as footsteps within a discretized area, and footsteps on stairs.

Chapter 5 Localization using Nearest Neighbors

5.1. Introduction

In this chapter, a vibration-based event localization method is considered using a nearest-neighbor machine learning approach for classification. The K-Nearest Neighbor (KNN) technique is implemented for location-based classification in an active building environment with a sparse sensor distribution and a low sampling rate (< 2kHz). A preliminary investigation is performed on a small section of hallway to locate hammer strikes, ball drops, and footsteps. The good accuracy prompted the use of the more sophisticated KNN method. This method is first used to locate footsteps in a hallway experiment, and then used to locate footsteps on a staircase. In both scenarios, three accelerometers are used to classify the location of the source from a grid of possible locations. This method can provide localization with few sensors and low sampling rates, requiring significantly fewer data to be aquiered compared to previous methods. The tradeoff, however, is with developing an appropriately sized training set, which can increase computation times if left unrestricted. While the computation time is not the focus of this study, it should be considered for large scale application.

5.2. Hallway Experiment

The first experiment is performed to determine whether footsteps can be differentiated based on location. In this section, the testing process is discussed, and a tool for preliminary

investigation is developed. A further analysis follows using KNN, based on the good results of the preliminary study.

5.2.1. Setup and Procedure

Experimental data was collected on the 3rd floor of Goodwin Hall, a five-story steel-framed building with concrete floors on the Virginia Tech campus [55, 126]. The setup shown in Figure 1 is part of a corridor within the active building. Tape was used to create a 4 m^2 square grid divided into 16 sections. The testing area was set up in a corner of the building, at the intersection of two outward facing walls within a hallway. Three accelerometers (PCB 393B04) were placed at 3 of the four corners, 5 cm away from the grid. The accelerometers were attached to the floor with adhesive wax. Each square is assigned a representative number, the order of which corresponds to the path taken for the walking study. Measurements were made using an NI 9234 module with MATLAB's Data Acquisition Toolbox on a Dell Latitude E6530 laptop. The NI 9234 was selected due to its built-in anti-aliasing and ability to power the IEPE accelerometers used. The sampling rate was set to 1860 S/s. The system was set to trigger based on the amplitude of each channel independently, using the sensor with the largest amplitude as the reference. Custom functions were written for both data acquisition and classification. The floor was excited by hammer strikes, table-tennis ball drops, and footsteps within the grid. For the hammer strikes and ball drops, each cell within the grid was impacted 16 times. Each impact occurred by hand, and was generally confined toward the center of the cell. For footstep excitation, three people walked along the path following the squares numbered 1 to 16 shown in Figure 1a. Shoes were removed prior to walking to reduce the variance caused by footwear. Participants were asked to maintain steps to within each square

section and prevent steps from overlapping multiple grids simultaneously. Each participant walked the path four times, resulting in a total of 192 footsteps. A 6th order band-pass Butterworth filter with cutoff frequencies at 10 Hz and 840 Hz was used to reduce the effects of background noise.

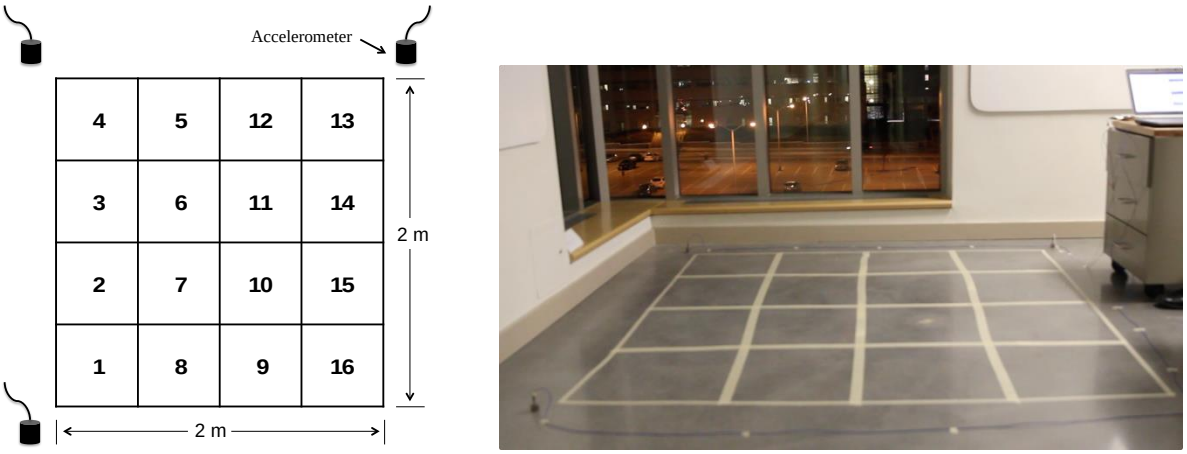

(a) (b)

Figure 5.1. (a) Sketch of the test-setup and numbering system; (b) testing area on the 3nd floor. The numbering system corresponds to the path taken for the walking study.

5.2.2. Classification method

As a preliminary study, a supervised learning approach based on the nearest neighbor is employed to classify the location of the event. Leave-one-out-cross-validation is used to assess the classification accuracy. Previous research and details of this technique can be found in [124, 125]. The validation process is as follows: for both the ball-drop and hammer-strike measurements, one response from each location is left out (16 hammer-strikes or ball-drops), and the remaining 240 responses are used as the training set. This leaves 15 training samples for each location. The same process is used for footsteps, leaving out one of the 12 walk-trials (16 footsteps) and assigning the remaining 176 footsteps for the training set. To implement the classification technique, a training set must be constructed. Each of the M total members of the training set construct each row of the $M \times N$ matrix as,

$$\mathbf{H} = \begin{bmatrix} \mathrm{H}_{1,1}, & \dots, & \mathrm{H}_{1,N} \\ \vdots, & \mathrm{H}_{i,n}, & \vdots \\ \mathrm{H}_{M,1} & \dots, & \mathrm{H}_{M,N} \end{bmatrix}. \tag{5.1}$$

The elements of **H** are described using the index notation $\mathrm{H}_{i,n}$ for the n^{th} column (sample) of the i^{th} row (signal) in the matrix **H**. A 2-dimensional coordinate is assigned for each of the M members in **H** that corresponds with the known source location, and used to construct the $M \times 2$ coordinate matrix

$$\mathbf{C} = \begin{bmatrix} x_1, & y_1 \\ \vdots, & \vdots \\ x_M, & y_M \end{bmatrix}. \tag{5.2}$$

Once an impact occurs at an unknown location, the measured response R_n is cross-correlated with each signal within the training set and used to construct the $M \times (2N - 1)$ correlation matrix

$$\mathbf{D} = \begin{bmatrix} \mathbf{d}_1 \\ \vdots \\ \mathbf{d}_\mathrm{M} \end{bmatrix}. \tag{5.3}$$

Each row i of **D** is calculated as,

$$\mathbf{d}_{i,} = \sum_{k=1}^{N} \mathrm{T}_{i,n-k} R_k. \tag{5.4}$$

where $\mathbf{d}$ is the vector of length $2N-1$ that results from the cross-correlation, and $\mathbf{d}_i$ is the i^{th} vector (row) in matrix $\mathbf{D}$. The matrix $\mathbf{D}$ now contains the measured signal after it has been cross-correlated with each member of the training set. To find the member of the training set that is most like the measured signal, the maximum value b_i for each row within $\mathbf{D}$ is obtained as

$$b_i = \max\left(\mathrm{D}_{i,n}\right), \tag{5.5}$$

and used to construct the correlation vector

$$\mathbf{b} = \begin{bmatrix} b_1 \\ \vdots \\ b_M \end{bmatrix}. \tag{5.6}$$

Finally, the maximum value within the vector $\mathbf{b}$ corresponds to the member of the training set that is most similar to the measured response. The row of the maximum value, given by

$$\mathrm{p} = \arg\max_i(\mathrm{b}_i) \tag{5.8}$$

is used to find the predicted location $\mathbf{z}$ as

$$\mathbf{z} = \left[\mathrm{C}_{\mathrm{p},1}, \mathrm{C}_{\mathrm{p},2}\right] \tag{5.9}$$

where the $\mathrm{C}_{i,j}$ terms are the previously defined components of the coordinate matrix $\mathbf{C}$. This is equivalent to a nearest-neighbor search (NNS) approach, taking the location of the training sample

with the largest correlation value as the location of the incoming data. Since three sensors are used in this study, Eqs. (1-9) are repeated for each sensor to obtain three possible locations: $\mathbf{z}_1, \mathbf{z}_2, \mathbf{z}_3$. These three classifications are resolved to a single point using a voting scheme. In circumstances where no location has more than a single vote (i.e., each sensor returns a unique coordinate), then the average over each dimension (x, y) is taken. For example, if each location is treated as a member of the set

$$\Phi = \{\mathbf{z}_1, \mathbf{z}_2, \mathbf{z}_3\}, \tag{5.10}$$

and $f(\phi)$ is the probability mass function, then the resolved coordinate $\mathbf{g}$ is

$$\mathbf{g} = \begin{cases} \frac{\mathbf{z}_1+\mathbf{z}_2+\mathbf{z}_3}{3}, & f(\phi) = 1, \phi \in \Phi \\ \arg\max\big(f(\phi)\big), & f(\phi) > 1, \phi \in \Phi \end{cases}. \tag{11}$$

This method is ad-hoc, and was created as a straightforward way to resolve the classification algorithm when there are discrepancies among sensor classifications.

5.2.3. Preliminary Results

The accuracy of the classification method is measured by the distance (measured in steps) between the true location and the predicted location of the event. Figure 2 shows the results for each of the three scenarios: hammer strikes, ball drops, and footsteps. Both the ball drops and hammer strikes are correctly located in 100% of the tests. The results are different for footsteps,

with 56% being correctly located, and 92% located to within 1 step (equivalent to one step distance error) of the true location.

Figure 5.2. Occurrence rate as a function of localization accuracy for the hallway experiment using the custom classification method.

The results for footstep localization are promising, although expectedly worse than the accuracy seen with both the hammer strike and ball drop tests. The differences are likely due to the larger physical variance of footstep excitation incurred in each step and between each candidate. The relative consistency of hammer strikes and ball drops allows the differences in the measured signal to be primarily a product of the location relative to the sensors. With footsteps, both the location and the physical variance come into play, making the measured response more difficult to accurately classify.

5.2.4. Further Analysis

An ensemble subspace KNN approach was implemented using MATLAB to classify the location of footsteps. While there are many methods with which to perform machine learning, the preliminary analysis suggested that a KNN approach performs well. The approach consists of training the algorithm on a selected set of training data, and evaluating the performance on a set of testing data. For this data segmentation, there were two scenarios of interest. The first scenario

is when various portions of all the available data are used. In this scenario, the various portions used for testing data are 20%, 30%, and 40%. For each portion, the testing data is randomly selected from the full data set. The remaining data for each scenario is used to train the algorithm. This selection range was chosen to see how much data would be required to train the classifier. The second scenario is when vibration measurements from an occupant have not been used to train the classification algorithm, and are instead used to test the classifier.

Once both the training set and the testing set have been defined, the training set is used to develop the classification algorithm. First, the number of neighbors required to model the data was determined by cross-validation. The cross-validation process used a KNN model based on the training data for an arbitrary number of folds. The resulting loss factor (i.e., failure rate) is determined for a range of neighbors, and the number of neighbors associated with the least loss factor is selected. The use of 1 nearest neighbor was found to be optimal in all scenarios. Second, ensembles for the nearest neighbor classifications were created. The dimension of the subspace ensemble is randomly varied and the resulting cross validation loss is examined. The other parameters such as the number of folds and the size of the ensemble are kept constant. The third step was to determine smallest number of learners that can be used to classify the data and give a low correlation error. In most cases, using fewer learners corresponds with lower memory requirements.

5.2.5. Results and discussion

The results are shown in Figure 5.3 for each portion of data left out for testing, along with the averaged results from leaving out each person. The accuracy overall appears worse in all 4

cases compared to the previous method used for preliminary analysis. This is likely due to the amount of data used for training versus testing. In the preliminary analysis, only 8% of the data was left out for testing at any given time. Additionally, the number of correctly located footsteps decreased as the amount of data left out for testing increased.

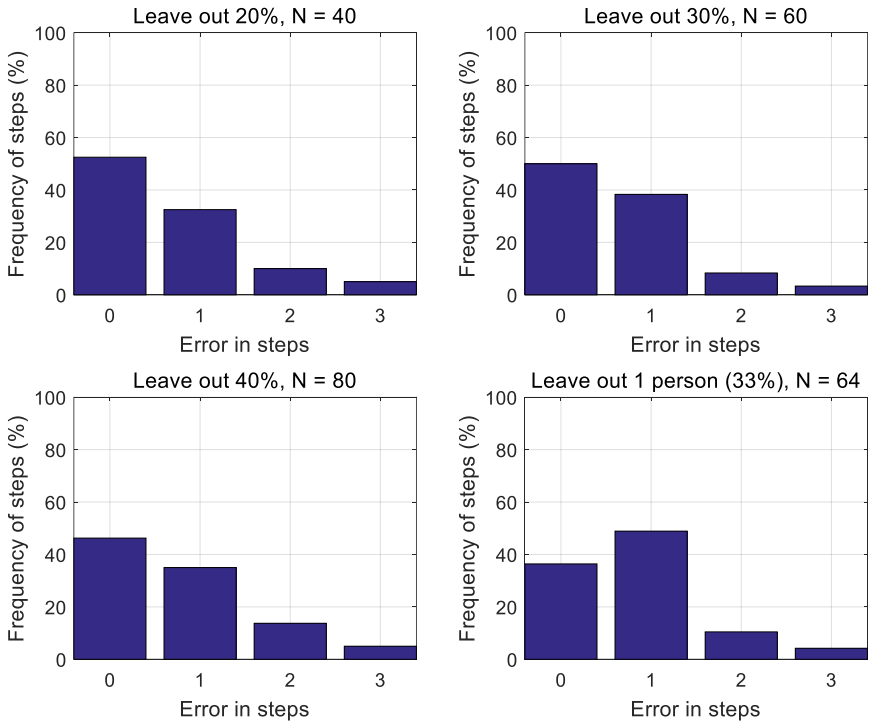

Figure 5.3. Occurrence rate as a function of localization accuracy for the hallway experiment using the KNN algorithm.

The number of misclassifications to 1 step away increased when testing an occupant who is not in the training data. This is misfortunate, although expected due to the inherent differences in walking styles. Overall, the results show good accuracy and the direct dependency on the training set . In all cases, the footsteps were located to within 1 step over 80% of the time, regardless of the amount of data used. For the case where 30% of the data is left for testing, the number of footsteps poorly located (i.e., greater than 1 step away) is at a minimum of 12%. The

reason for this is not exactly known, or if there is any physical significance. Leaving a person out provided the fewest correct classifications, but still 85% were located to within 1 step. A summary table of the results for each case is shown in Table 5.1.

Table 5.1. Summary of the localization results for the hallway experiment.

Test details	Size of testing data	Correct location classified	Within 1 step	> 1 step
Leave a person (8%)	64/192	36%	85%	15%
Leave 20%	40/192	70%	80%	20%
Leave 30%	60/192	50%	88%	12%
Leave 40%	80/192	46%	81%	19%

5.3. Staircase Experiment

The second experiment is performed to on stairs. The individual steps of a stair case provide a natural discretization, where the possible footstep locations are not as structurally coupled as they are with a floor. In this section, the testing process is discussed, and the previous analysis using KNN is repeated.

5.3.1. Setup and procedure

Experimental data is collected on a stairwell between the 4th and 5th floors of Goodwin Hall. The setup is shown in Figure 5.4. Each of the 12 stair steps are used for classification purposes. The same three accelerometers used in the previous experiment (PCB 393B04) are placed on the edges of the 2nd, 7th, and 12th steps using adhesive wax. Each step is assigned a representative number from 1 to 12. Measurements were made using the same NI 9234 module

with MATLAB's Data Acquisition Toolbox as with the previous experiment. The sampling rate was kept at 1860 S/s. Six people were asked to walk along the stairs. Data collection was performed separately for each climb and descent of the stairs. The participants were signaled to walk up the stairs, and wait at the top for the next signal to begin walking back down. This process was repeated five times for each of the six participants, totaling 720 footsteps. A 6th order high-pass Butterworth filter with a cutoff frequency at 37 Hz was found to be effective for classification. The high-pass filter helped remove a significant portion of the low frequency dynamics of the staircase that were being recorded.

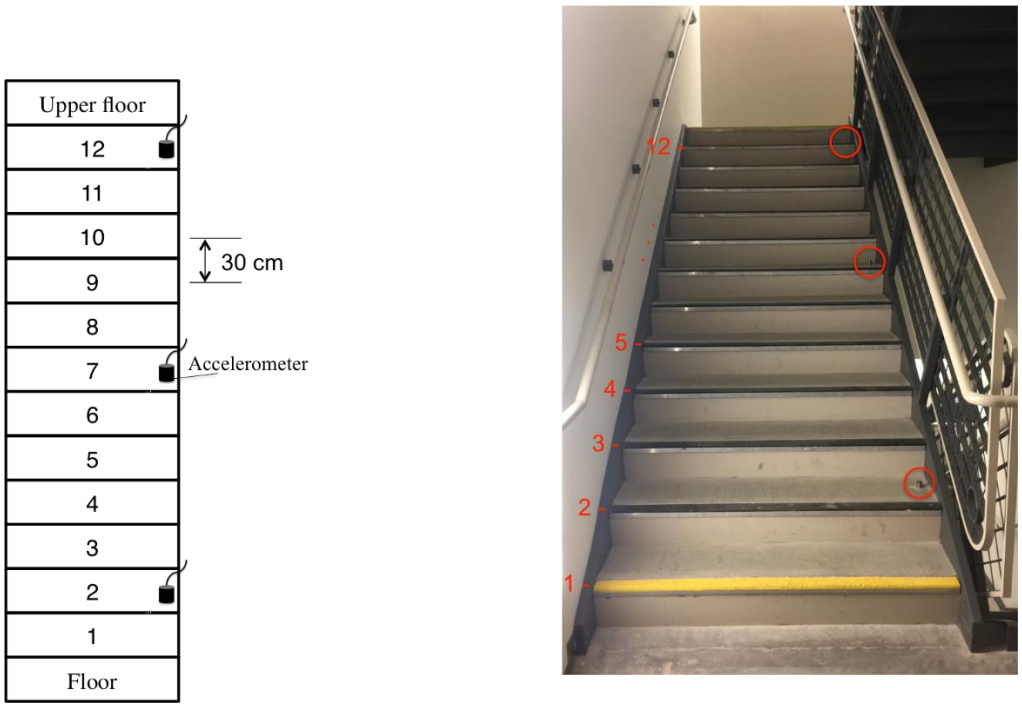

(a) (b)

Figure 5.4. Stairwell used for tests located between the 4th and 5th floors of Goodwin Hall. Steps are numbered 1-12. Accelerometers are placed on the 2nd, 6th, and 11th steps.

5.3.2. Results

The same KNN method used for analysis in the first experiment is implemented again here. Due to the larger potential distance error in this experiment (11 as opposed to 3), the accuracy is also considered for cases where the error is 2 steps or fewer. Figure 5.5 shows a graphical representation of the different outcomes for the various cases. As with the previous study, the number of correct classifications decreased as the amount of data left out increased. Additionally, the number of misclassifications increased when testing an occupant who is not in the training data set. The overall outcomes are better in this experiment, which makes intuitive sense considering the natural discretization provided by each step. There is a structural physical difference of each stair step (making the reading more unique per step) and there is an enforced physical constraint (the user is forced to step in more controlled discrete points) that the other tests did not provide. In the scenarios where a portion of the data was left out, over 80% of all footsteps were correctly located out of the 12 possible steps. This number reduces significantly 66% in the case where a person is left out, which is similar to what was found in the hallway experiment. Considering footsteps that are located within 2 steps, the case where 20% of the data is left out, provides the best results of 97%. The other cases are accurate to about 90% as well. A summary table of the results for each case is shown in Table 5.2.

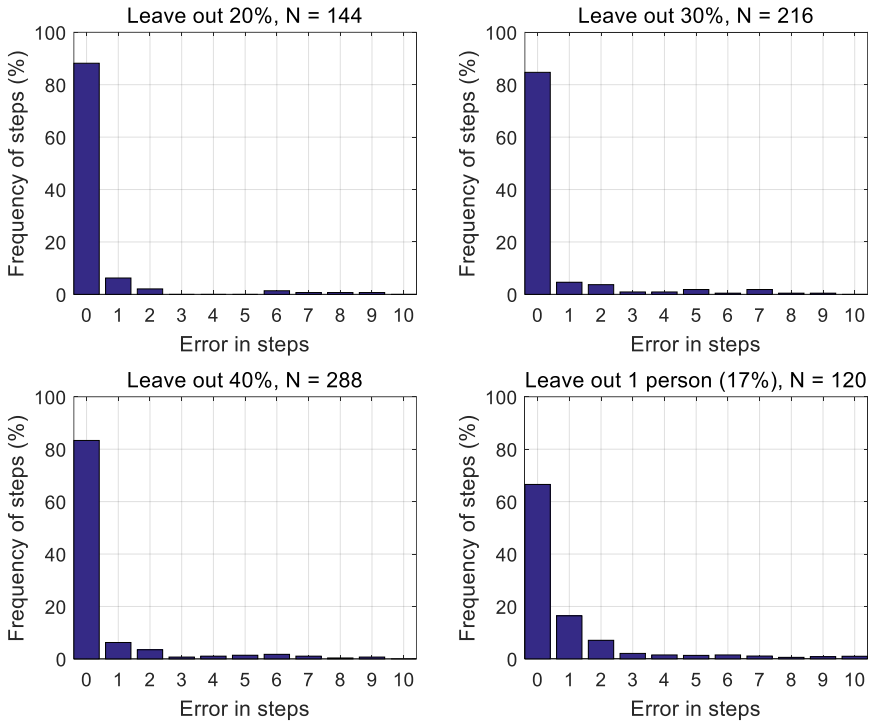

Figure 5.5. Occurrence rate as a function of localization accuracy for the staircase experiment using the KNN algorithm.

Table 5.2. Summary of the localization results for the staircase experiment.

Test details	Size of testing data	Correct location classified	Within 1 step	Within 2 steps	> 2 steps
Leave a person (17%)	120/720	66%	75%	88%	12%
Leave 20%	144/720	88%	94%	97%	3%
Leave 30%	216/720	85%	89%	93%	7%
Leave 40%	288/720	83%	90%	93%	7%

5.4. Discussion

The preliminary analysis for the hallway experiment provided a first look at the effectiveness of a nearest neighbor approach to localization. The effect of the physical variance

provided by footsteps was well observed in this experiment. Hammer strikes and ball drops were perfectly located, while the footstep results were lower. Despite this, the results were sufficient to warrant further analysis and experiments. The KNN algorithm provided a more sophisticated approach for classification and analysis. Consistent with the nearest neighbor method used initially, the KNN algorithm provided the best results when only 1 neighbor was considered. This is somewhat intuitive, as the physical nature of the problem is highly variable in nature. Using more neighbors can average the physical variance and result in higher proportion of misclassified footsteps. Locating footsteps on the staircase expectedly provided higher accuracy than in the hallway. Not surprisingly, using a larger training set resulted in better classification results in all scenarios. This may imply that the data set used is insufficient in size to fully evaluate the classification method used. Similarly, when measurements from an occupant's footsteps were not in the data set, the performance significantly decreased. This makes sense, and suggests that any occupant whose footsteps have not been measured would be more difficult to locate. This could allude to the fact that a training set capable of spanning the space of footsteps has not been reached and the training set needs to be increased. Further evaluation of this could yield a more consistent solution with a convergence in needed training sets such that all the variances have been captured and the robustness of the method ensued. It is also likely that with a higher sampling rate, features such as the time-difference between sensors may be used to potentially yield more accurate results.

The results suggest that the approach could be feasible in areas where a training set can be readily obtained. The simplistic excitation method of the hammer and ball-drop tests performed favorably compared to the more sophisticated footstep excitation. While the results

are promising, further analysis would be needed to show the accuracy of footsteps in a more natural walking environment (i.e. not trying to step within squares).

5.5. Conclusion

This chapter implements a nearest neighbor approach to classify the location of footsteps in an indoor building. Experiments are carried out both in a hallway and on a staircase within an operational building. Vibration measurements are made for several types of floor excitation (ball-drop, hammer-strike, footstep) and classified using matched filters and a nearest-neighbor search. The results show perfect accuracies in classifying the ball-drops and hammer strikes, but a decreased accuracy for the walking trials, which is likely due to the higher variance of footsteps compared to the other impacts. Further analysis showed a slight relationship between the amount of data used for training compared to accuracy. The largest factor was found to be whether an occupant's measurements are available in the training set. Relative to other methods, this technique uses a low sampling rate (1860 S/s) and requires few sensors, however, it also requires the use of a training set, which in some cases might not be possible. To further test the practicality of this method, future work should consider this approach in a less controlled environment, such as exciting the gridded area with no knowledge of the grid boundaries. Additionally, this method could be implemented using a training set developed with an excitation method other than the one being classified. With these additions, the feasibility of practical implementation would become more apparent.

In the next chapter, a novel bipod design for single-sensor, one-dimensional bearing estimation is introduced. The design is implemented in a beam simulation and used to determine

from which side the beam is impacted. Initial design functionality is evaluated and several configurations are investigated for performance.

Chapter 6 Bipod for Bidirectional Bearing Estimation

6.1. Introduction

This chapter investigates a novel instrumentation method for bearing estimation in 1-D systems via simulation. More specifically, the work examines a novel approach and the feasibility of using a single sensor to determine the direction of arrival (DOA) of a propagating waveform in a solid beam. The goal is to provide the initial framework for single-sensor bearing estimation by considering the effects of an asymmetric sensor-structure interface. This is a simplified version of the bearing estimation problem, where the solution in 2-D space is a unit vector pointing towards the source. Bearing estimation is a commonly implemented component of emission-source localization. For radially symmetric waves in 2-D space, obtaining a bearing estimate requires a minimum of two independent sensors. A reduction in the required number of sensors implies the obvious cost-savings benefit of reduced hardware requirements, while also allowing for more redundancy in localization problems. The next section discusses this novel concept in more detail, followed by a description of the model used for simulations.

6.2. Concept and Sensor-Structure

A multi-point coupling method is proposed to resolve bidirectional ambiguity of waves propagating in symmetric, elastic solids by incorporating an asymmetric bipod at the point of instrumentation. Previous methods that resolve bidirectional ambiguity use a minimum of two sensors, but are also capable of 2-D bearing estimation. This research investigates only bidirectional ambiguity, but lays the fundamental understanding that can be extended to single-sensor bearing estimation. This technique is assessed in a simulation environment with different joint configurations compared and discussed. Effects of uncorrelated white noise are also considered. Future applications of this research can be expanded to develop more advanced sensor designs that use multi-point coupling to effectively imitate multiple bandwidth-limited sensors. This research intends to lay the groundwork for using advanced coupling systems to allow individual sensors to behave in a multi-sensor fashion by exploiting the sensor-structure connection point of the sensor.

In summary, the proposed coupling method attempts to differentiate between the DOA of a propagating waveform with a single sensor by inducing asymmetry at the sensor-structure interface via a small bipod. Acceleration measurements are taken from the apex of an asymmetric bipod, where an accelerometer would be placed in an experimental setting. By introducing asymmetry, the propagated waveform may be differentiated based on the DOA. For example, consider the concept drawing shown in Figure 6.1. A wave traveling along the beam would excite the sensor at both interface locations. Ignoring any coupling between the two interface points, the sensor would first measure the wave as it propagates through the first interface. After a time delay the wave would pass through the soft interface and excite the sensor a second time. This would result in measuring the same signal twice, with some amplitude and phase shift, which would be dependent on the transfer functions induced by the bipod and the interface points. If it is assumed

that there is no dispersion, and the soft connection provides only damping, then a wave propagating from the rigid side would first see the full signal strength, followed by the damped version of the same signal as it passes through the soft connection. If the wave originates from the soft side, a lower energy representation of the signal would arrive first, followed by an amplified version as it passes through the rigid connection. In this example, the DOA would be easily distinguishable using a time domain representation by simply observing which characteristic response is measured first.

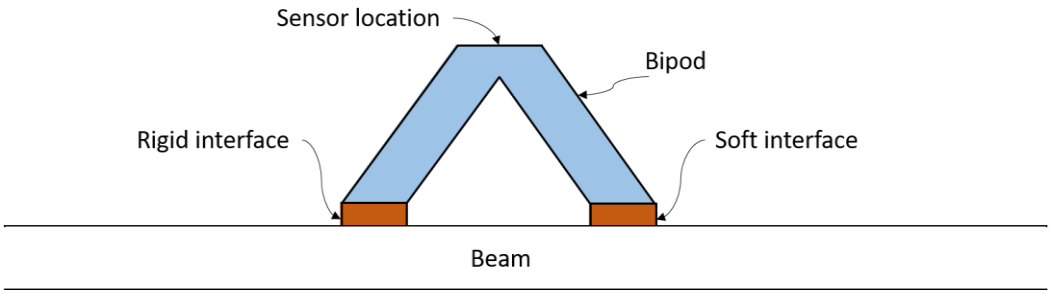

Figure 6.1. Concept sketch of the asymmetric bipod design.

With a more realistic representation, inputs from the rigid side of the bipod would couple to the soft side, creating a more complex time-trace. The differences, however distinguishable, would be present within the response. It is the purpose of this research to investigate the distinguishability and compare the results to simply asymmetrically instrumenting the structure (i.e. placing the sensor off-center).

In a dispersive medium the wave train is much more complex due to the nonlinear relationship between frequency and wavenumber, and thus the DOA distinction may not be easily identified by visual inspection. There are many ways in which the temporal difference may be

evaluated to determine the DOA, and would depend on the specific characteristics of the coupled joint. This research applies a simple method based on matched filtering using a set of training points and correlation coefficients.

The developed method is applied to a beam model using randomly selected impact locations. The accuracy is used to assess the initial concept, as well as a variety of geometry configurations. The results are discussed within the context of localization and future applications are considered. The following section will discuss the model used for simulation, followed by a series of investigative simulations. The correlation approach is then developed, followed by a feasibility study. Lastly, the geometry of the bipod is considered.

6.3. Concept evaluation

In this section, the bipod concept is defined, and several investigative studies are performed.

6.3.1. Model

A model is developed to investigate the performance and accuracy of the proposed asymmetric coupling method. This will be used to determine the DOA of impacts occurring on the left side ($x < 0$) or right side ($x > 0$) of a beam. The model represents a 20 in. long beam instrumented with a bipod, shown in Figure 6.2. The bipod is structurally coupled to two points on a beam ($x = \pm 2$ in.) equidistant from the centerline ($x = 0$). To introduce asymmetry, the left leg of the bipod is connected rigidly to the beam while the right leg is connected using a 6 Degree of Freedom (DOF) spring with a stiffness of 100 lbf/in.

The material properties of the beam are selected to match estimates for medium density fiberboard (MDF). The beam has a width of 2 in. and a thickness of 0.5 in, and is discretized using 800 CBEAM [127] elements with an element size of 0.025 inches. The bipod is 2 inches tall and 4 inches wide, resulting in each leg having a length of $\sqrt{8}$ in. (2.824 in.).

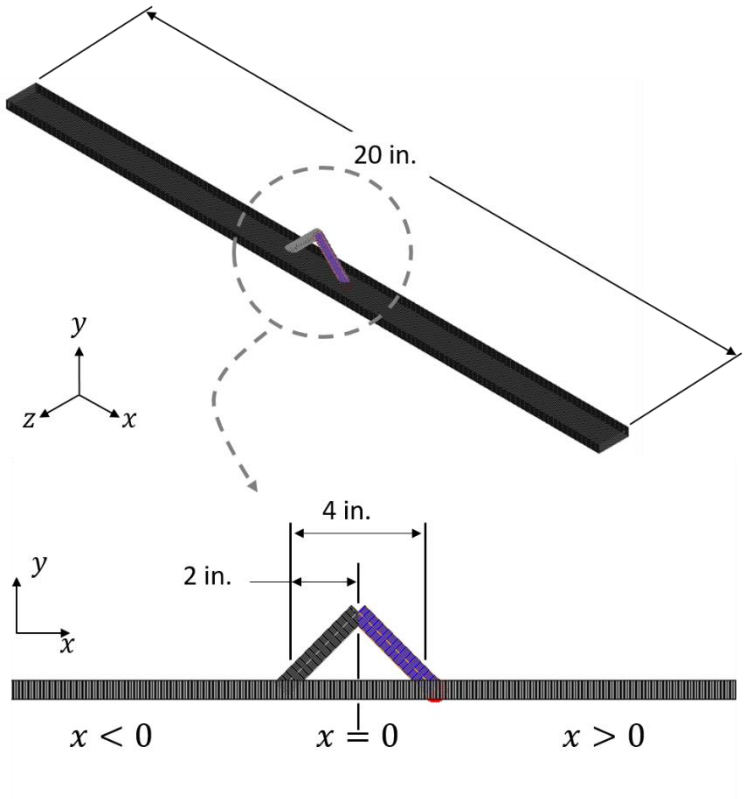

Figure 6.2. Model of the beam with bipod used for simulations. The geometry of the right leg (purple) is varied, along with the stiffness of the connection to the beam (red).

Each leg has a square cross-section with a side length of 0.5 in., and is modeled with 57 CBEAM elements with an element spacing of 0.0496 inches. This results in a model composed of 914 Beam elements and one spring element with six degrees of freedom. The full model contains 5478 degrees of freedom and is simulated using MSC Nastran Direct Transient Response. A unit impulse time-dependent excitation is used to excite the system at a single point for each simulation.

The solution is solved at 3001 time steps, with $\Delta t = 0.1$ ms resulting in a total evaluated response time of 300 ms. The acceleration response is measured from the apex of the bipod, effectively mimicking accelerometer measurements at that location while neglecting any mass loading effects.

6.3.2. Initial Study

To get a first look at the differences in waves travelling from one side or the other, simulations are carried out for impacts at either end ($x = \pm L/2$) and the responses are compared. It was initially expected that this test would provide sufficient time and/or frequency information to develop a method that resolves the bidirectional ambiguity passively. The results, shown in Figure 6.3 show the difference in the responses can be identified by visual inspection. The largest difference occurs in the first 10 to 15 ms. The differences, however, are minor and ambiguous; they do not provide a straight-forward route to passive implementation. To investigate this further, a correlation method is developed in the next section to compare impacts from one side of the beam to the other.

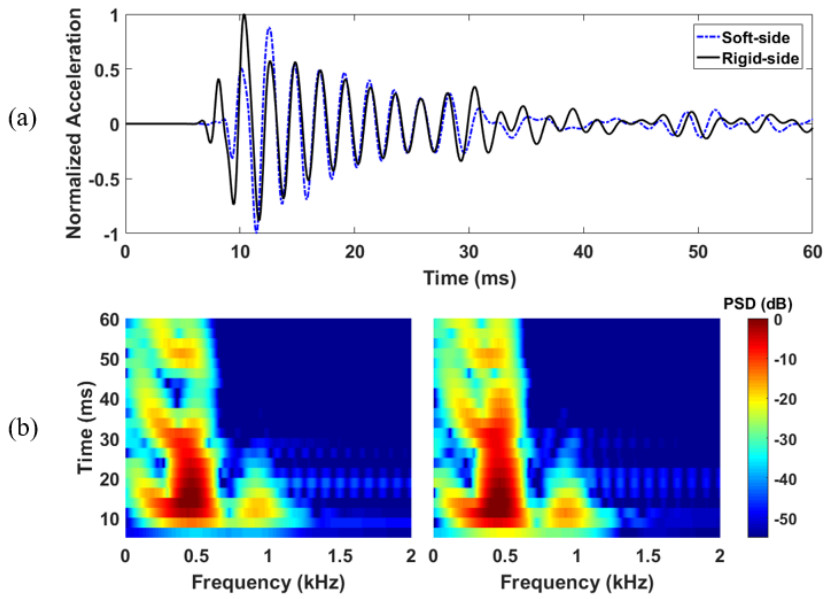

Figure 6.3. Time-traces (a) and spectrograms (b) of impacts occurring at either end of the beam. The spectrograms show the differences between impacts on the soft side (left) and rigid side (right).

6.3.3. Twelve-Point Cross-Correlation

A correlation approach is developed under the assumption that impacts from one side of the beam tend to be more similar to each other than they are to impacts on the other side of the beam. Developing this approach begins by comparing the response of impulses equally spaced along the beam to each other. Twelve impulse locations are selected, with each side of the beam having 6 impulses equally spaced (3 in. apart) starting from each of the end boundaries. The number of training points was arbitrarily selected to be reasonable relative to the size of the model. A normalized cross-correlation approach is used to make the comparisons, with only the maximum value of the correlation considered. For each impulse location k, the correlation coefficient c_k is calculated

$$c_k(n) = \max\left(\int_{-\infty}^{\infty} \hat{w}_k(t)\, \hat{w}_n(t-\tau)\; d\tau\right), \tag{5.1}$$

where t is the time vector, and $\hat{w}(t)$ is the l^2-normalized version of the impulse response at either location k or n. This results in 12 correlation coefficients for each of the 12 impulse locations. The maximum correlation always occurs when $k = n$, since this is when the signal is being correlated with itself, and will always have a value of 1. The results are shown in Figure 6.4, where the maximum correlation coefficient for each impact combination is shown.

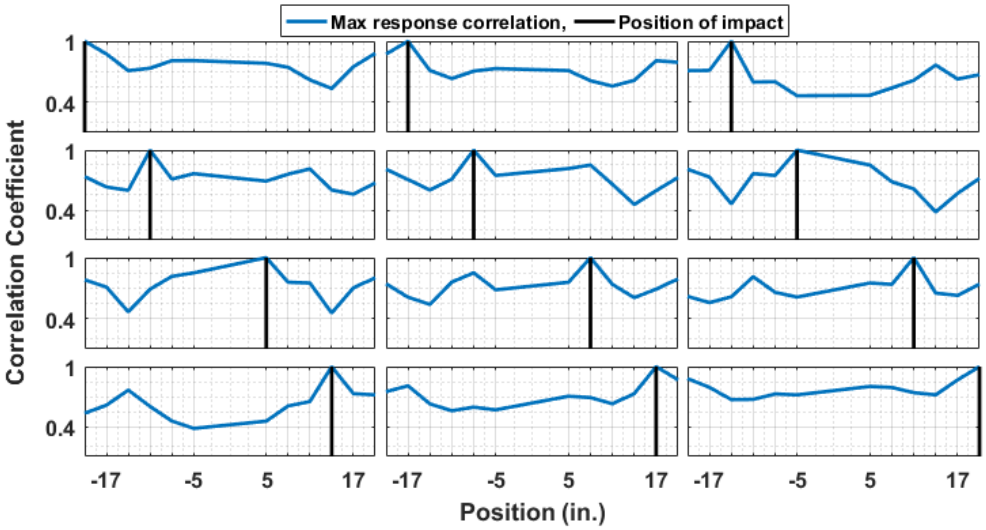

Figure 6.4. Correlation results using Eq. (5.1) for each of the 12 impulses along the beam. Acceleration measurements are taken from the top of the bipod.

From the results, the symmetry in the beam can be readily recognized. While each impact response correlates most highly with itself, the response from the symmetric point on the opposite side tends to have a relatively high value as well. It may also be noted that responses from the same side as the trial impact tend to correlate better with the trial impact than their symmetric

counterparts. This observation suggests the total area under the curve for each side of the beam will be greater for the side in which the impact originated.

6.3.4. Comparison to asymmetric sensor placement

A critical function of the bipod is to perform better than simply instrumenting the beam at an asymmetric location. This provides supporting evidence for the usefulness of the bipod substructure. To do this, the acceleration response of the beam is measured without the bipod, at what would be the rigid location of the bipod ($x = -2\ in$). This is equivalent to instrumenting the beam with an accelerometer at an asymmetric location (without the effects of mass loading). This is again evaluated with Eq. (5.1), and the results shown in Figure 6.5 suggest a weak correlation between impacts occurring along the same side of the beam. This implies a sum-total of cross-correlation coefficients would likely not be as effective. There is also a noticeable difference in the average correlation value across all impact points, being much lower in this case than they were in the case with the bipod.

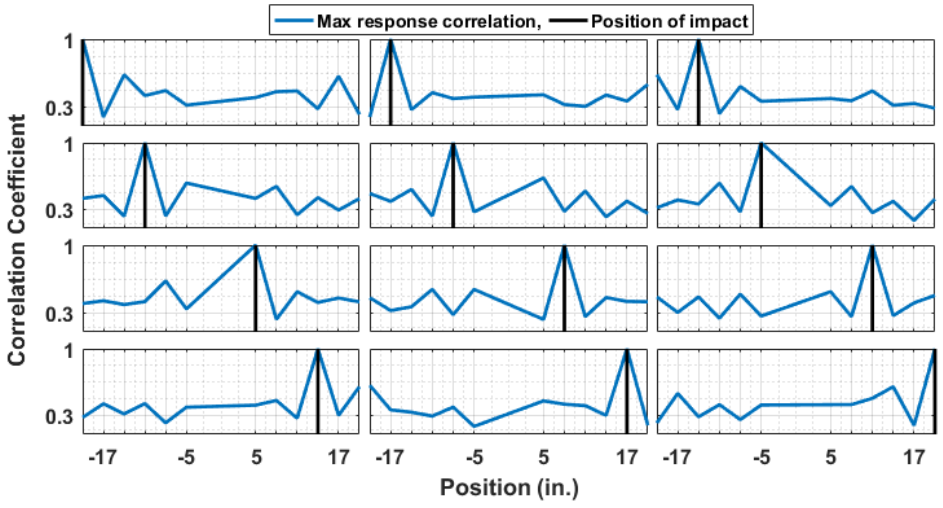

Figure 6.5. Correlation results using Eq. (5.1) for each of the 12 impulses along the beam. Acceleration measurements are taken from $x = 2\ in.$ without the bipod present.

6.4. Bipod based DOA

A matched-filter approach is used to correlate the response from impact that occurs at an unknown location, $y(t)$, to a set of trial impacts, $w_n(t)$, that occur at known locations x_n. The unknown impact is compared to all trial impacts and the direction is determined based on the sum of maximum correlation. Each correlation value is formulated by taking the maximum of the cross-correlation between the unknown impact and the trial impacts. For a trial impact n, the correlation coefficient a_n is

$$a_n = \max\left(\int_{-\infty}^{\infty} \hat{y}(t)\ \hat{w}_n(t-\tau)\ d\tau\right) \tag{5.2}$$

where $\hat{y}(t)$ and $\hat{w}(t)$ are the L2-normalized versions of the simulated responses. The results from Eq. (5.2) are used to form the correlation vector:

$$\mathbf{A} = \begin{bmatrix} a_1 \\ a_2 \\ \vdots \\ a_n \end{bmatrix}. \tag{5.3}$$

For each trial impact w_n, a coefficient b_n is determined based on the location of the trial impact x_n:

$$b_n(x_n) = \begin{cases} -1, & x_n < 0 \\ 1, & x_n \geq 0 \end{cases} \tag{5.4}$$

and used to form the assignment vector

$$\mathbf{B} = \begin{bmatrix} b_1 \\ b_2 \\ \vdots \\ b_n \end{bmatrix}. \tag{5.5}$$

For each impact $y(t)$, a coefficient is calculated to determine the DOA:

$$\beta = \mathbf{B}^{\mathrm{T}}\mathbf{A} \tag{5.6}$$

where a value of $\beta > 0$ suggests the impact came from the right side, and similarly, a value of $\beta < 0$ suggests an origin of the left side. The next section evaluates the reliability of the asymmetric bipod to determine the DOA using the formulation in Eqs. (5.2-5.6) for randomly selected impacts.

6.4.1. Algorithm performance evaluation

Using the response from the previous 12 measurements as a training set, the developed matched filter approach is used to identify the DOA of 96 impacts at random locations along the length of the beam. Each impact is correlated with each of the 12 training points, and the originating side from which the new impact came from is determined by comparing the sum-total correlation for each respective side, i.e. Eq. (6). The results, shown in Figure 6.6, show good accuracy with the few training points used, with 92% of the 96 points accurately placed.

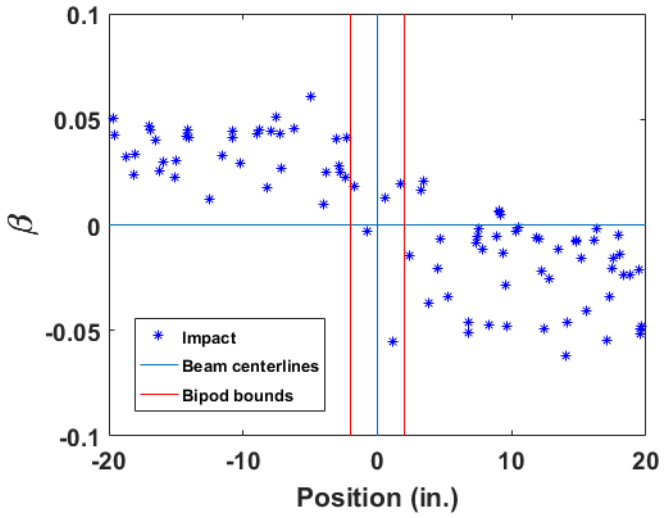

Figure 6.6. β results for each impact calculated from Eq. (5.6) for 96 randomly selected points along the beam with the bipod present. For values of $\beta > 0$, the impact is assumed to have occurred on the left side of the beam, while $\beta < 0$ suggests the impact occurred on the right side. The red lines show the bounds of the bipod.

The β values shown (in blue) correspond to the result from Eq. (6), and are placed at the location of the impact on the beam. The left and right bounds of the bipod are shown as vertical lines in red, with the centerlines of the beam shown in cyan. Values of $\beta > 0$ suggest the impact originated from the left side of the beam, while values of $\beta < 0$ suggest the impact came from the right.

Revisiting the case of asymmetric sensor placement, the bipod must perform better than simply measuring from an asymmetric location. The results of asymmetric sensor placement, without the bipod, are shown in Figure 6.7, where 75% of the 96 points are accurately placed. This suggests that the asymmetric bipod performs better to determine the DOA than using only asymmetric sensor placement. In the following section, the accuracy is again evaluated under several noise considerations.

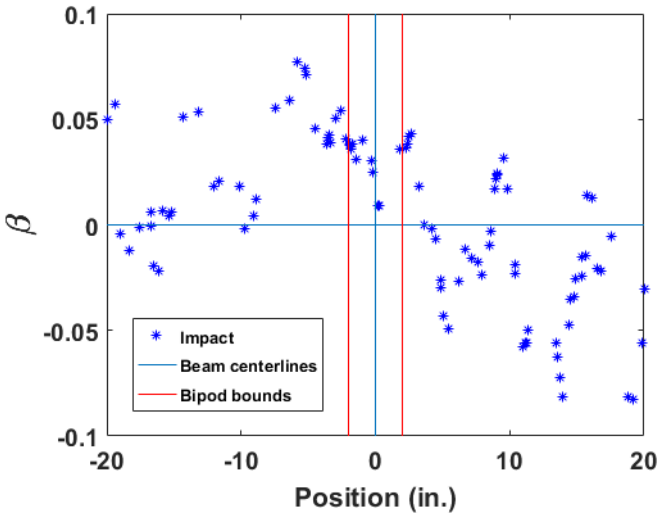

Figure 6.7. β results for each impact calculated from Eq. (5.6) for 96 randomly selected points along the beam without the bipod. Measurements are taken from asymmetric location ($x = -2\ in.$) along the beam.

6.5. Performance Evaluation

To more accurately represent a realistic environment, the process is again repeated but with the addition of white noise. Uncorrelated white noise is generated independently and added to each response from the training set and each response of the 96 impacts. The effect of noise is evaluated at several different noise power levels, using signal-to-noise ratios (SNR) of 10, 3, and 0 dB relative to the average energy of the training set. An example of the response at each noise level is provided in Figure 6.8 to give the reader an idea of how noisy the signal is in each case.

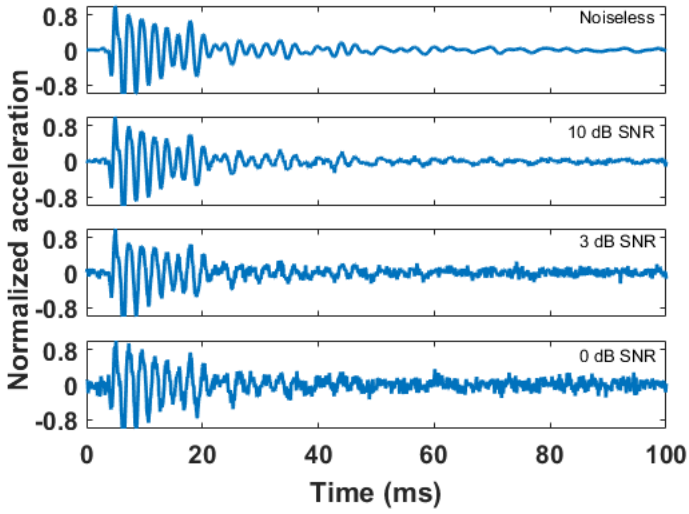

Figure 6.8. Response as measured from the apex of the bipod for an impact at *x = -8 in.*. Three noise cases are provided for reference: no 10, 3, and 0 dB SNR.

For each noise case, the accuracy in determining the correct DOA for the bipod is reduced from 92% to 88%, 73%, and 70%. For the case of measuring from an asymmetric location, the accuracy at 10 dB SNR is unchanged, and reduced from the noiseless case of 75% to 73% and 71% for SNRs of 3 dB and 0 dB, respectively. This suggests that with little to no noise, the bipod performs better than placing the sensor asymmetrically. With more noise this is no longer the case, and the bipod performs equally well to placing the sensor asymmetrically.

5.5.1. Adding additional training points

Revisiting the results in Figure 6.6, there are impact locations that do not perform well, and so there is interest in determining the effects of adding additional training points to the training set. A new training point is added at $x = 9.2$ in., and the 96 points are re-evaluated at all 3 noise intervals. The results from the noiseless case are shown in Figure 6.9 and have an accuracy of

95%, up from 92% with the original 12 training points. Adding noise up to an SNR of 10 dB does not affect the accuracy, but for SNRs of 3 dB and 0 dB the accuracy reduces to 94% and 83%. Adding a new point for the asymmetric sensor case increases accuracy to 81%, up from 75% with the original 12 training points. Similarly, the 10 dB SNR scenario did not affect accuracy, but for SNRs of 3 dB and 0 dB the accuracy reduces to 79% and 77%. As expected, the correlation method presented may be improved upon by adding additional training points in areas where accuracy is low. The results from this section are summarized in Table 6.1. In the next section, the effects of bipod geometry on accurately determining the DOA are considered.

Table 6.1. Summary of results for each setup and noise scenario in determining the DOA of 96 impacts. The case of asymmetric sensor placement is referred to as Asy. S.

Setup	Accuracy for locating 96 random impacts (%)							
	SNR without updating				SNR with updating			
	Noiseless	10 dB	3 dB	0 dB	Noiseless	10 dB	3 dB	0 dB
Bipod	92	88	73	70	95	95	94	83
Asy. S.	75	75	73	71	81	81	79	77

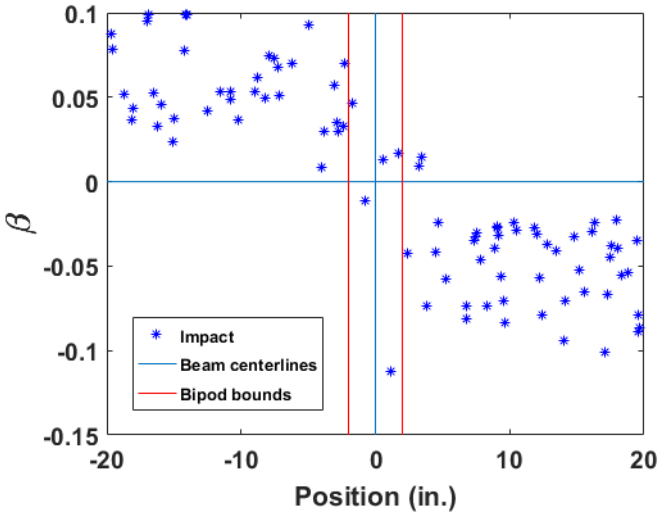

Figure 6.9. β results calculated from Eq. (5.6) for 96 randomly selected points along the beam with the bipod present. An additional training point has been added at $x = 9.2\ in$.

6.5.2. Geometry investigation

An initial study is carried out to determine the effects of the geometry of the joint on resolving the DOA of an impact. To simplify the geometric parameters, both bipod legs are changed to have a circular cross-section. The left ($x < 0$) leg is kept at a constant 0.25 in. radius with a rigid connection, while the right leg has variable stiffness and radius. The stiffness ranges from 10 lbf/in. to 50 kips/in. distributed over 12 points. Likewise, the radius is swept from 0.0417 in. to 0.5 in. This results in 144 design points for optimization. The stiffness and radius values for the variable leg are selected to have a range of interface properties that deviate significantly from those of the rigid connection.

For each of the 144 design points, the 96-point verification method previously described in section 7 is used. Each geometry and spring stiffness is evaluated based on overall accuracy using an SNR of 6 dB SNR. This SNR was selected as a "reasonable" amount of noise, although interpretations may vary based on application. The results from the parameter sweep are shown in Figure 6.10.

Varying the leg radius and spring stiffness shows the highest accuracy when the spring stiffness is relatively low, and the leg radius is greater than or equal to the 0.25 in. radius of the left leg. The initial, unmodified geometry at 6 dB SNR has an accuracy of 79%, and increases to up to 95% with the appropriate geometry modifications. This suggests that a properly designed bipod is much better than the case of asymmetrically placing a sensor (75%), even when noise is considered. A low accuracy region is found when both legs of the bipod have equal radius, and the

spring stiffness is high. In this region, the accuracy approaches 50%, which is equivalent to guessing. This is expected, because in this region both legs of the bipod are nearly identical, and the system is nearly symmetric. Interestingly, performance is poor when both the spring stiffness and leg radius are very low. This could be due to a vibration mode of the bipod dominating the response, but the reason is unclear.

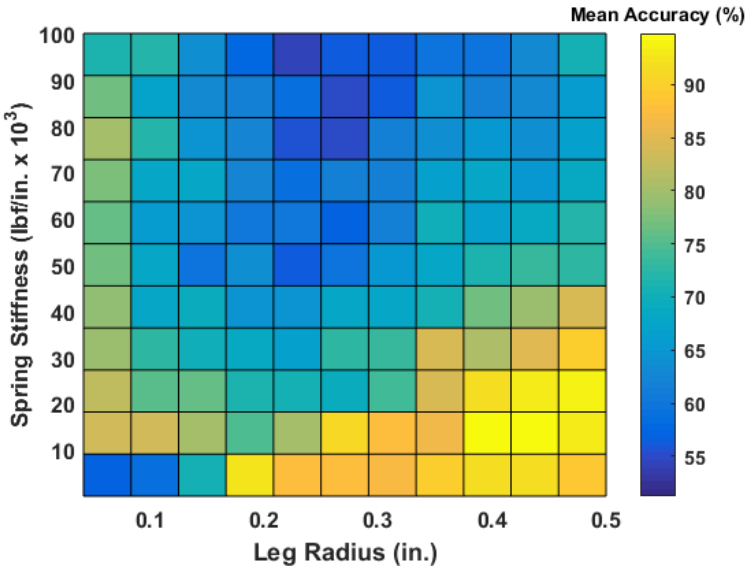

Figure 6.10. Average accuracy over a range of geometry and stiffness configurations for the right ($x > 0$) leg of the bipod. The maximum accuracy is 95% with a radius of 0.42 in. and a stiffness of 9.1 lbf/in.

6.6. Conclusion

In this chapter, an asymmetric coupling method is proposed as a tool to reduce bidirectional ambiguity of a wave propagating in a solid beam. The method utilizes a bipod that is coupled to the beam at two locations, with one location being rigidly coupled to the beam while the other is coupled using a 6DOF spring. The accuracy of determining the DOA is evaluated in a simulation environment. The performance is compared with instrumenting the beam at an asymmetric location. The asymmetric bipod instrumentation method is found to be effective in determining the DOA on a beam, more so than simply instrumenting the beam at an asymmetric location. The

differences are most prominent in the noiseless case, with 92% accuracy when using the asymmetric bipod compared to 75% when simply measuring at an off-center location. With a 10 dB noise level, the accuracy of the bipod reduces to 88%, while the off-center measurement case is unaffected at 75%, suggesting robustness to noise. No cases were found where measuring from an off-center location produced higher accuracy than the asymmetric bipod. Investigating the geometry configuration suggests the best accuracy can be achieved when the interface stiffness is low and the radius of the variable leg is large relative to the constant leg. In this region, an accuracy of 95% is achieved, despite a 6 dB SNR. This increase is compared to the original geometry, where the accuracy is 79%. It is probable that selecting a method for correlating signals with custom designed joint configurations would provide greater accuracy. The use of cross-correlation to determine the DOA was selected as a simple method to determine the overall similarity of the signals and evaluate the concept, it is likely that more sophisticated methods would yield greater accuracy. The results suggest the instrumentation method provides sufficient benefit to warrant further interest.

Chapter 7 Summary and Conclusion

7.1. Summary of Dissertation

This body of work herein investigates the problem and associated challenges of indoor footstep localization via vibration measurements. The physical nature of the problem is examined, and several techniques are investigated for their feasibility to solve the localization problem. Chapter 1 discusses prior literature and outlines the areas where contributions are most welcomed. In Chapter 2, the problem of footstep localization is discussed within the context of indoor buildings. A typical suspended building floor is considered within the context of plate dynamics, and the resulting dynamics are discussed from a localization perspective. The difficulties associated with using traditional localization techniques (such as those found in acoustics) are considered. The additional complexities added by various structural and non-structural building elements are examined for their impact on the localization problem. Several techniques implemented for plate localization are examined for their applicability to footsteps in an indoor building environment.

In Chapter 3, impacts on a plate are simulated and localization is performed using TDOA. Two TDOA techniques are implemented and the large errors are used to show the difficulties in implementing TDOA in this environment. Various wave speeds are used to show that there is no assumed wave velocity that works well for all locations due to the dispersive nature of the problem. The effects of reflections are also considered by examining the sign-of-arrival for potential use with the SO-TDOA algorithm.

Chapter 4 carries out an experiment in an instrumented building, where hammer impacts are located using multiple methods. The measurements made from the hammer impacts are used to estimate the dispersion properties of the building floor. Localization is performed using two TDOA methods. Dispersion compensation is furthermore implemented via TDDM, and its effects on accuracy are compared to the traditional TDOA methods. In each case, several parameters are also investigated for their effects on accuracy.

In Chapter 5, a machine learning approach to localization is implemented based on location classification. Training data is used to inform a K-Nearest Neighbor approach, which is then used to locate various impacts as well as footsteps within Goodwin Hall. Various parameters are optimized based on the training data prior to classification. Experiments are carried out in two different locations within the building. The first experiment is carried out in a small section of a hallway, while the second experiment is performed on a staircase. To our knowledge this is the first attempt to apply such techniques to a staircase localization study.

The efforts applied to define the structural localization problem outlined in Chapter 2 led to the concept of a novel instrumentation method. Chapter 6 discusses the use of a structurally asymmetric bipod, which interfaces between the sensor and the floor, for localization while reducing the amount of needed sensors. A preliminary investigation of the bipod design is performed via a finite element simulation of a beam. The bipod, with a single sensor, is used to determine the DOA of a propagating waveform. The geometric parameters of the bipod are investigated for their effects on the accuracy of the DOA estimation.

7.2. Summary of Contribution

This work lays a foundation for using vibration measurements for indoor footstep localization with a focus on the structural components affecting the problem at hand. The physical nature of the problem is defined, and the associated difficulties and limitations which must be overcome are outlined. Several of these difficulties are highlighted in a plate simulation, where multiple time-difference approaches are compared. A machine learning approach to footstep localization is also implemented, which showed an inverse relationship between the likelihood of classification and the prediction error in addition to promising accuracy. A dispersion compensation approach to localization is implemented in a building with structural instrumentation, which showed an increase in localization accuracy as well as additional room for further improvement. Separately, a novel instrumentation method is designed to provide directional inference from a single point of measurement.

7.3. Areas for Future Work

The use of vibration measurements for footstep localization has only recently received significant interest. Being a relatively new field, there are many areas for further contribution, including the expansion of the work presented herein. The two methods implemented in this work are the use of dispersion compensation techniques discussed in Chapter 4, and the machine learning approach from Chapter 5.

Dispersion compensation generally requires the dispersive properties of the media to be known. This is something that was estimated in Chapter 4, but is not extensively investigated. Performing a more thorough analysis of indoor building dispersion is a daunting task, requiring

extensive testing and measurements. Nevertheless, it would provide the benefit of having a real-world example of the dispersive characteristics, which can be further incorporated into the assumptions commonly made for indoor localization. Aside from implementing dispersion compensation, certain techniques (e.g., [120]) rely on the consistency of dispersion throughout the media. While it is already established that the dispersion is inconsistent, the extent of these inconsistencies is not fully defined, and does not have any real-world examples.

A machine learning approach to localization can have a potentially unlimited number of avenues for future work. The method implemented here used a discretization system for localization, but could benefit greatly from a larger scale investigation. As well, more sophisticated processing techniques may be implemented. Chapter 5 showed that when the classifier was not trained on an occupant's footsteps, then the associated prediction error increased. This prediction error was different for each occupant, suggesting that some footsteps were worse than others for training. It would be of use to investigate this further, and determine if there may be some generic impulse that can be used as an input that will work well for classifying the location of footsteps. Further, the size of the investigated area performed in this research is small, but provided promising results. Investigating the use of the KNN approach for a much larger area would be of interest.

Aside from the methods presented in this research, there are many more avenues for footstep localization which may be investigated. Chapter 2 outlines several techniques that were originally implemented for plate localization that have applicability to building floors (e.g., [121]).

Bibliography

1. FCC, *(15-9) Wireless E911 Location Accuracy Requirements*. 2015.
2. P. Torcellini, S.P., M. Deru, B. Griffith, N. Long, R. Judkoff, *Lessons learned from case-studies of six high-performance buildings,* in *Technical Report NREL/RP-550-37542*. 2006.
3. Zhang, J., et al., *Energy savings for occupancy-based control (OBC) of variable-air-volume (VAV) systems.* PNNL-22072, 2013: p. 1-79.
4. Mao, G., B. Fidan, and B.D. Anderson, *Wireless sensor network localization techniques.* Computer networks, 2007. **51**(10): p. 2529-2553.
5. Athalye, A., et al. *A radio frequency identification system for accurate indoor localization*. in *Acoustics, Speech and Signal Processing (ICASSP), 2011 IEEE International Conference on*. 2011. IEEE.
6. Foxlin, E., *Pedestrian tracking with shoe-mounted inertial sensors.* IEEE Computer graphics and applications, 2005. **25**(6): p. 38-46.
7. Li, F., et al., *A reliable and accurate indoor localization method using phone inertial sensors,* in *Proceedings of the 2012 ACM Conference on Ubiquitous Computing*. 2012, ACM: Pittsburgh, Pennsylvania. p. 421-430.
8. Nam, Y., *Map-based Indoor People Localization using an Inertial Measurement Unit.* Journal of Information Science and Engineering, 2011. **27**(4): p. 1233-1248.
9. Colombo, A., et al. *A wearable embedded inertial platform with wireless connectivity for indoor position tracking*. in *Instrumentation and Measurement Technology Conference (I2MTC), 2011 IEEE*. 2011. IEEE.

10. Adib, F., Z. Kabelac, and D. Katabi. *Multi-Person Localization via RF Body Reflections*. in *NSDI*. 2015.

11. Encarnação, P., *Footstep localization based on in-home microphone-array signals.* Assistive Technology: From Research to Practice: AAATE 2013, 2013. **33**: p. 90.

12. Kaddoura, Y., J. King, and A. Helal. *Cost-Precision Tradeoffs in Unencumbered Floor-Based Indoor Location Tracking*. in *International conference on smart homes and health telematics; From smart homes to smart care*. 2005. Sherbrooke, Quebec, Canada.

13. Sousa, M., et al. *Human Tracking and Identification using a Sensitive Floor and Wearable Accelerometers*. in *IEEE International Conference on Pervasive Computing and Communications (PerCom)*. 2013.

14. Peck, L. and J. Lacombe. *Seismic-based personnel detection*. in *Security Technology, 2007 41st Annual IEEE International Carnahan Conference on*. 2007. IEEE.

15. Xing, H.-F., F. Li, and Y.-L. Liu. *Wavelet denoising and feature extraction of seismic signal for footstep detection*. in *Wavelet Analysis and Pattern Recognition, 2007. ICWAPR'07. International Conference on*. 2007. IEEE.

16. Mehmood, A., T. Damarla, and J. Sabatier, *Separation of human and animal seismic signatures using non-negative matrix factorization.* Pattern Recognition Letters, 2012.

17. Damarla, R. and D. Ufford. *Personnel detection using ground sensors*. in *Defense and Security Symposium*. 2007. International Society for Optics and Photonics.

18. Dibazar, A.A., et al., *Intelligent Recognition of Acoustic and Vibration Threats for Security Breach Detection, Close Proximity Danger Identification, and Perimeter Protection*. 2011, DTIC Document.

19. Park, H.-O., A.A. Dibazar, and T.W. Berger. *Cadence analysis of temporal gait patterns for seismic discrimination between human and quadruped footsteps*. in *Acoustics, Speech and Signal Processing, 2009. ICASSP 2009. IEEE International Conference on*. 2009. IEEE.

20. Houston, K.M. and D.P. McGaffigan. *Spectrum analysis techniques for personnel detection using seismic sensors*. in *AeroSense 2003*. 2003. International Society for Optics and Photonics.

21. Bland, R.E., *Acoustic and seismic signal processing for footstep detection*. 2006, Massachusetts Institute of Technology.

22. Jin, X., et al. *Symbolic dynamic filtering of seismic sensors for target detection and classification*. in *American Control Conference (ACC), 2011*. 2011. IEEE.

23. Iyengar, S.G., P.K. Varshney, and T. Damarla. *On the detection of footsteps based on acoustic and seismic sensing*. in *Signals, Systems and Computers, 2007. ACSSC 2007. Conference Record of the Forty-First Asilomar Conference on*. 2007. IEEE.

24. Subramanian, A., et al., *A data-driven personnel detection scheme for indoor surveillance using seismic sensors.* Unattended Ground, Sea, and Air Sensor Technologies and Applications XI. SPIE, 2009. **7333**: p. 733315.

25. Ekimov, A. and J.M. Sabatier, *Vibration and sound signatures of human footsteps in buildings.* The Journal of the Acoustical Society of America, 2006. **120**: p. 762.

26. Sabatier, J.M. and A.E. Ekimov. *Range limitation for seismic footstep detection*. in *SPIE Defense and Security Symposium*. 2008. International Society for Optics and Photonics.

27. Sabatier, J. and A. Ekimov. *A review of human signatures in urban environments using seismic and acoustic methods*. in *Technologies for Homeland Security, 2008 IEEE Conference on*. 2008. IEEE.

28. Hamilton, J., et al., *Characterization of human motion through floor vibration*, in *Dynamics of Civil Structures, Volume 4*. 2014, Springer. p. 163-170.

29. DeLoney, C., *Person identification and gender recognition from footstep sound using modulation analysis.* 2008.

30. Itai, A. and H. Yasukawa. *Footstep recognition with psyco-acoustics parameter*. in *Circuits and Systems, 2006. APCCAS 2006. IEEE Asia Pacific Conference on*. 2006. IEEE.

31. Itai, A. and H. Yasukawa. *Personal Identification Using Footstep Based on Wavelets*. in *Intelligent Signal Processing and Communications, 2006. ISPACS'06. International Symposium on*. 2006. IEEE.

32. Itai, A. and H. Yasukawa. *Footstep classification using wavelet decomposition*. in *Communications and Information Technologies, 2007. ISCIT'07. International Symposium on*. 2007. IEEE.

33. Itai, A. and H. Yasukawa. *Footstep classification using simple speech recognition technique*. in *Circuits and Systems, 2008. ISCAS 2008. IEEE International Symposium on*. 2008. IEEE.

34. Mehmood, A., V.M. Patel, and T. Damarla. *Discrimination of bipeds from quadrupeds using seismic footstep signatures*. in *Geoscience and Remote Sensing Symposium (IGARSS), 2012 IEEE International*. 2012. IEEE.

35. Miyoshi, M., et al. *Personal identification method using footsteps*. in *SICE Annual Conference (SICE), 2011 Proceedings of*. 2011. IEEE.

36. Shoji, Y., T. Takasuka, and H. Yasukawa. *Personal identification using footstep detection*. in *Intelligent Signal Processing and Communication Systems, 2004. ISPACS 2004. Proceedings of 2004 International Symposium on*. 2004. IEEE.

37. Pakhomov, A., et al. *Seismic footstep signal characterization*. in *AeroSense 2003*. 2003. International Society for Optics and Photonics.

38. Bales, D., et al., *Gender Classification of Walkers Via Underfloor Accelerometer Measurements.* IEEE Internet of Things Journal, 2016.

39. Bales, D., et al., *Gender Classification Using Under Floor Vibration Measurements,* in *Dynamics of Coupled Structures, Volume 4*. 2016, Springer. p. 377-383.

40. Times, N.Y. *Attention, Shoppers: Store Is Tracking Your Cell*. 2013 [cited 2017 22 Jun].

41. Kuroiwa, J., *Vibration tests of a multistory building*. 1967, California Institute of Technology.

42. Foutch, D., et al. *Full scale three-dimensional tests of structural deformations during forced excitation of a nine-story reinforced concrete building*. in *Proceedings, US National Conference on Earthquake Engineering*. 1975.

43. Trifunac, M.D., *Comparisons between ambient and forced vibration experiments.* Earthquake Engineering and Structural Dynamics, 1972. **1**(2): p. 133-150.

44. Kohler, M.D., P.M. Davis, and E. Safak, *Earthquake and ambient vibration monitoring of the steel-frame UCLA Factor building.* Earthquake Spectra, 2005. **21**(3): p. 715-736.

45. Safak, E. and K. Hudnut. *Real-time structural monitoring and damage detection by acceleration and GPS sensors*. in *8th US national conference on earthquake engineering, San Francisco, California*. 2006.

46. Foti, D., et al., *Ambient vibration testing, dynamic identification and model updating of a historic tower.* NDT & E International, 2012. **47**: p. 88-95.

47. Brownjohn, J.M., et al., *Dynamic and static response of Republic Plaza.* Journal-Institution of Engineers Singapore, 1998. **38**: p. 35-41.

48. Brownjohn, J.M., *Structural health monitoring of civil infrastructure.* Philosophical Transactions of the Royal Society of London A: Mathematical, Physical and Engineering Sciences, 2007. **365**(1851): p. 589-622.

49. Lee, H., J.W. Park, and A. Helal, *Estimation of indoor physical activity level based on footstep vibration signal measured by MEMS accelerometer in smart home environments*, in *Proceedings of the 2nd international conference on Mobile entity localization and tracking in GPS-less environments*. 2009, Springer-Verlag: Orlando, FL, USA. p. 148-162.

50. Pan, S., et al. *BOES: building occupancy estimation system using sparse ambient vibration monitoring*. in *SPIE Smart Structures and Materials+ Nondestructive Evaluation and Health Monitoring*. 2014. International Society for Optics and Photonics.

51. Pan, S., et al. *Occupant traffic estimation through structural vibration sensing*. in *SPIE Smart Structures and Materials+ Nondestructive Evaluation and Health Monitoring*. 2016. International Society for Optics and Photonics.

52. Bahroun, R., et al., *New algorithm for footstep localization using seismic sensors in an indoor environment.* Journal of Sound and Vibration, 2014. **333**(3): p. 1046-1066.

53. Poston, J.D., et al. *Indoor positioning from vibration localization in smart buildings*. in *2016 IEEE/ION Position, Location and Navigation Symposium (PLANS)*. 2016. IEEE.

54. Poston, J.D., et al. *Towards indoor localization of pedestrians via smart building vibration sensing*. in *Localization and GNSS (ICL-GNSS), 2015 International Conference on*. 2015. IEEE.

55. Schloemann, J., et al., *Vibration Event Localization in an Instrumented Building*, in *Experimental Techniques, Rotating Machinery, and Acoustics, Volume 8*. 2015, Springer. p. 265-271.

56. Poston, J.D., et al. *Vibration sensing in smart buildings*. in *Proc. Int. Conf. Indoor Position. Indoor Navig.(IPIN)*. 2015.

57. Hamilton, J., *Design and implementation of vibration data acquisition in Goodwin Hall for structural health monitoring, human motion, and energy harvesting research*, in *Mechanical Engineering*. 2015, Virginia Tech.

58. Pakhomov, A., et al. *Single-and three-axis geophone: footstep detection with bearing estimation, localization, and tracking*. in *AeroSense 2003*. 2003. International Society for Optics and Photonics.

59. Richman, M.S., et al. *Personnel tracking using seismic sensors*. in *Aerospace/Defense Sensing, Simulation, and Controls*. 2001. International Society for Optics and Photonics.

60. Succi, G.P., et al. *Problems in seismic detection and tracking*. in *AeroSense 2000*. 2000. International Society for Optics and Photonics.

61. Poston, J.D., R.M. Buehrer, and P.A. Tarazaga, *Indoor footstep localization from structural dynamics instrumentation.* Mechanical Systems and Signal Processing, 2017. **88**: p. 224-239.

62. Akaike, H., *A new look at the statistical model identification.* IEEE transactions on automatic control, 1974. **19**(6): p. 716-723.

63. Mirshekari, M., et al. *Characterizing wave propagation to improve indoor step-level person localization using floor vibration*. in *SPIE Smart Structures and Materials+ Nondestructive Evaluation and Health Monitoring*. 2016. International Society for Optics and Photonics.

64. Daubechies, I., *The wavelet transform, time-frequency localization and signal analysis.* IEEE transactions on information theory, 1990. **36**(5): p. 961-1005.

65. Tobias, A., *Acoustic-emission source location in two dimensions by an array of three sensors.* Non-destructive testing, 1976. **9**(1): p. 9-12.

66. Lenz, C., *Localization of Sound Sources Studies on Mechatronics.* 2009.

67. Moré, J.J., *The Levenberg-Marquardt algorithm: implementation and theory*, in *Numerical analysis*. 1978, Springer. p. 105-116.

68. Chan, Y. and K. Ho, *A simple and efficient estimator for hyperbolic location.* Signal Processing, IEEE Transactions on, 1994. **42**(8): p. 1905-1915.

69. Knapp, C. and G. Carter, *The generalized correlation method for estimation of time delay*. IEEE Transactions on Acoustics, Speech, and Signal Processing, 1976. **24**(4): p. 320-327.

70. Falati, S., *The contribution of non-structrual components to the overall dynamic behaviour of concrete floor slabs*. 1999, University of Oxford.

71. Kram, R., et al., *Force treadmill for measuring vertical and horizontal ground reaction forces.* Journal of Applied Physiology, 1998. **85**(2): p. 764-769.

72. Graff, K.F., *Wave motion in elastic solids*. 1975: Courier Dover Publications.

73. De Marchi, L., et al., *A passive monitoring technique based on dispersion compensation to locate impacts in plate-like structures.* Smart Materials and Structures, 2011. **20**(3): p. 035021.

74. Ziola, S.M. and M.R. Gorman, *Source location in thin plates using cross-correlation.* The Journal of the Acoustical Society of America, 1991. **90**(5): p. 2551-2556.

75. Kerr, S.C., *Human induced loading on staircases*. 1998, University of London.

76. Mercier, H., et al., *Vibration problems in structures: practical guidelines*. 2012: Birkhäuser.

77. Smith, A.L., S.J. Hicks, and P.J. Devine, *Design of floors for vibration: A new approach*. 2007: Steel Construction Institute Ascot, Berkshire, UK.

78. Whittle, M.W., *Generation and attenuation of transient impulsive forces beneath the foot: a review.* Gait & posture, 1999. **10**(3): p. 264-275.

79. Racic, V., A. Pavic, and J. Brownjohn, *Experimental identification and analytical modelling of human walking forces: literature review.* Journal of Sound and Vibration, 2009. **326**(1): p. 1-49.

80. Giakas, G. and V. Baltzopoulos, *Time and frequency domain analysis of ground reaction forces during walking: an investigation of variability and symmetry.* Gait & Posture, 1997. **5**(3): p. 189-197.

81. Simon, S.R., et al., *Peak dynamic force in human gait.* Journal of biomechanics, 1981. **14**(12): p. 817821-819822.

82. Willford, M., P. Young, and C. Field. *Improved methodologies for the prediction of footfall-induced vibration*. in *Optics & Photonics 2005*. 2005. International Society for Optics and Photonics.

83. Watters, B., *Impact-Noise Characteristics of Female Hard-Heeled Foot Traffic.* The Journal of the Acoustical Society of America, 1965. **37**(4): p. 619-630.

84. Keller, T., et al., *Relationship between vertical ground reaction force and speed during walking, slow jogging, and running.* Clinical Biomechanics, 1996. **11**(5): p. 253-259.

85. Alleyne, D.N. and P. Cawley, *The interaction of Lamb waves with defects.* IEEE transactions on ultrasonics, ferroelectrics, and frequency control, 1992. **39**(3): p. 381-397.

86. Lee, B. and W. Staszewski, *Modelling of Lamb waves for damage detection in metallic structures: Part II. Wave interactions with damage.* Smart Materials and Structures, 2003. **12**(5): p. 815.

87. Lowe, M.J., D.N. Alleyne, and P. Cawley, *Defect detection in pipes using guided waves.* Ultrasonics, 1998. **36**(1-5): p. 147-154.

88. Lowe, M.J., et al., *The low frequency reflection characteristics of the fundamental antisymmetric Lamb wave a 0 from a rectangular notch in a plate.* The Journal of the Acoustical Society of America, 2002. **112**(6): p. 2612-2622.

89. Pavic, A., Z. Miskovic, and P. Reynolds, *Modal testing and finite-element model updating of a lively open-plan composite building floor.* Journal of Structural Engineering, 2007. **133**(4): p. 550-558.

90. Pavic, A. and P. Reynolds, *Vibration serviceability of long-span concrete building floors. Part 1: Review of background information.* Shock and Vibration Digest, 2002. **34**(3): p. 191-211.

91. De Silva, S.S. and D.P. Thambiratnam, *Dynamic characteristics of steel–deck composite floors under human-induced loads.* Computers & Structures, 2009. **87**(17): p. 1067-1076.

92. Howard, C. and C. Hansen, *Vibration analysis of waffle floors.* Computers & structures, 2003. **81**(1): p. 15-26.

93. Reynolds, P., *The effects of raised access flooring on the vibrational performance of long-span concrete floors*. 2000, University of Sheffield.

94. Jeong, H. and Y.-S. Jang, *Fracture source location in thin plates using the wavelet transform of dispersive waves.* IEEE transactions on ultrasonics, ferroelectrics, and frequency control, 2000. **47**(3): p. 612-619.

95. Sharif-Khodaei, Z., M. Ghajari, and M. Aliabadi, *Determination of impact location on composite stiffened panels.* Smart Materials and Structures, 2012. **21**(10): p. 105026.

96. Wu, E., J.-C. Yeh, and C.-S. Yen, *Identification of impact forces at multiple locations on laminated plates.* AIAA journal, 1994. **32**(12): p. 2433-2439.

97. Harley, J.B. and J.M. Moura. *Broadband localization in a dispersive medium through sparse wavenumber analysis*. in *Acoustics, Speech and Signal Processing (ICASSP), 2013 IEEE International Conference on*. 2013. IEEE.

98. Ing, R.K., et al., *In solid localization of finger impacts using acoustic time-reversal process.* Applied Physics Letters, 2005. **87**(20): p. 204104.

99. Sekine, H. and S. Atobe, *Identification of locations and force histories of multiple point impacts on composite isogrid-stiffened panels.* Composite Structures, 2009. **89**(1): p. 1-7.

100. Choi, K. and F.-K. Chang, *Identification of impact force and location using distributed sensors.* AIAA journal, 1996. **34**(1): p. 136-142.

101. Jang, B.W., et al., *Real-time impact identification algorithm for composite structures using fiber Bragg grating sensors.* Structural Control and Health Monitoring, 2012. **19**(7): p. 580-591.

102. Kosel, T., I. Grabec, and F. Kosel, *Intelligent location of simultaneously active acoustic emission sources: Part I.* Aircraft Engineering and Aerospace Technology, 2003. **75**(1): p. 11-17.

103. Park, J., S. Ha, and F.-K. Chang, *Monitoring impact events using a system-identification method.* AIAA journal, 2009. **47**(9): p. 2011-2021.

104. Seydel, R. and F. Chang. *Implementation of a real-time impact identification technique for stiffened composite panels*. in *Proceedings of the 2nd International Workshop on Structural Health Monitoring*. 1999.

105. Seydel, R. and F.-K. Chang, *Impact identification of stiffened composite panels: I. System development.* Smart Materials and Structures, 2001. **10**(2): p. 354.

106. Worden, K. and W. Staszewski, *Impact location and quantification on a composite panel using neural networks and a genetic algorithm.* Strain, 2000. **36**(2): p. 61-68.

107. Mallat, S., *A wavelet tour of signal processing*. 1999: Academic press.

108. Meo, M., et al., *Impact identification on a sandwich plate from wave propagation responses.* Composite structures, 2005. **71**(3): p. 302-306.

109. Wilcox, P.D., *A rapid signal processing technique to remove the effect of dispersion from guided wave signals.* Ultrasonics, Ferroelectrics and Frequency Control, IEEE Transactions on, 2003. **50**(4): p. 419-427.

110. Sicard, R., J. Goyette, and D. Zellouf, *A numerical dispersion compensation technique for time recompression of Lamb wave signals.* Ultrasonics, 2002. **40**(1): p. 727-732.

111. Liu, L. and F. Yuan, *A linear mapping technique for dispersion removal of Lamb waves.* Structural Health Monitoring, 2010. **9**(1): p. 75-86.

112. Cai, J., et al., *High spatial resolution imaging for structural health monitoring based on virtual time reversal.* Smart Materials and Structures, 2011. **20**(5): p. 055018.

113. De Marchi, L., et al. *Dispersion compensation of Lamb waves with the warped frequency transform in passive monitoring techniques*. in *Ultrasonics Symposium (IUS), 2010 IEEE*. 2010. IEEE.

114. Perelli, A., et al., *Acoustic emission localization in plates with dispersion and reverberations using sparse PZT sensors in passive mode.* Smart Materials and Structures, 2012. **21**(2): p. 025010.

115. Kundu, T., S. Das, and K.V. Jata, *Detection of the point of impact on a stiffened plate by the acoustic emission technique.* Smart Materials and Structures, 2009. **18**(3): p. 035006.

116. Coverley, P. and W. Staszewski, *Impact damage location in composite structures using optimized sensor triangulation procedure.* Smart materials and structures, 2003. **12**(5): p. 795.

117. Ciampa, F. and M. Meo, *Acoustic emission source localization and velocity determination of the fundamental mode A0 using wavelet analysis and a Newton-based optimization technique.* Smart Materials and Structures, 2010. **19**(4): p. 045027.

118. Gaul, L. and S. Hurlebaus, *Identification of the impact location on a plate using wavelets.* Mechanical Systems and Signal Processing, 1998. **12**(6): p. 783-795.

119. Gaul, L. and S. Hurlebaus, *Determination of the impact force on a plate by piezoelectric film sensors.* Archive of Applied Mechanics, 1999. **69**(9): p. 691-701.

120. Park, J.-H. and Y.-H. Kim, *Impact source localization on an elastic plate in a noisy environment.* Measurement Science and Technology, 2006. **17**(10): p. 2757.

121. Ciampa, F. and M. Meo, *A new algorithm for acoustic emission localization and flexural group velocity determination in anisotropic structures.* Composites Part A: Applied Science and Manufacturing, 2010. **41**(12): p. 1777-1786.

122. Graff, K.F., *Wave motion in elastic solids*. 2012: Courier Corporation.

123. Allen, D.M., *The relationship between variable selection and data agumentation and a method for prediction.* Technometrics, 1974. **16**(1): p. 125-127.

124. Geisser, S., *The predictive sample reuse method with applications.* Journal of the American Statistical Association, 1975. **70**(350): p. 320-328.

125. Stone, M., *Cross-validatory choice and assessment of statistical predictions.* Journal of the Royal Statistical Society. Series B (Methodological), 1974: p. 111-147.

126. Hamilton, J.M., *Design and implementation of vibration data acquisition in Goodwin Hall for structural health monitoring, human motion, and energy harvesting research.* 2015.

127. Nastran, M., *Quick reference guide.* MSC. SOFTWARE, 2004. **1**.